



Ricerca di Sistema elettrico

Crescita da sospensioni di nanoparticelle di film sottili di CZTS per dispositivi fotovoltaici

N. Ataollahi, F. Bazerla, C. Malerba,
R. Di Maggio, A. Mittiga, P. Scardi

CRESCITA DA SOSPENSIONI DI NANOPARTICELLE DI FILM SOTTILI DI CZTS PER DISPOSITIVI FOTOVOLTAICI

N. Ataollahi¹, F. Bazerla¹, C. Malerba^{1,2}, R. Di Maggio¹, A. Mittiga², P. Scardi¹

¹ Università di Trento, DICAM, ² ENEA

Settembre 2018

Report Ricerca di Sistema Elettrico

Accordo di Programma Ministero dello Sviluppo Economico - ENEA

Piano Annuale di Realizzazione 2017

Area: Generazione di Energia Elettrica con Basse Emissioni di Carbonio

Progetto B.1.2: Ricerca su Tecnologie Fotovoltaiche Innovative

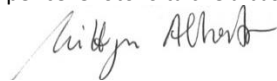
Obiettivo: Celle solari a base di film sottili innovativi di perovskiti e kesteriti – Subtask a.2 “Celle a singola giunzione a base di $\text{Cu}_2\text{ZnSnS}_4$ (CZTS)”

Responsabile del Progetto: Paola Delli Veneri, ENEA



Il presente documento descrive le attività di ricerca svolte all'interno dell'Accordo di collaborazione “Crescita e caratterizzazione chimica, morfologica e strutturale di film sottili per celle fotovoltaiche a base di semiconduttori Cu2-II-IV-VI4 ”

Responsabile scientifico ENEA: Alberto Mittiga



Responsabile scientifico Università di Roma: Paolo Scardi

Indice

SOMMARIO.....	4
1 INTRODUCTION.....	5
2 STUDY ON SYNTHESIS AND POST-ANNEALING OF $\text{Cu}_2\text{ZnSnS}_4$ ABSORBER LAYERS BASED ON OLEYLAMINE/1-DODECANETHIOL.....	5
2.1 EXPERIMENTAL PART.....	7
2.1.1 <i>Synthesis of CZTS NCs using DEG and TETA (K1)</i>	7
2.1.2 <i>Synthesis of CZTS NCs using OLA-1-DDT (K2)</i>	8
2.1.3 <i>Thin film deposition</i>	9
2.1.4 <i>NCs and thin films characterization</i>	10
3.1 RESULTS AND DISCUSSION.....	11
3.1.1 <i>Part a: synthesis of CZTS NCs using DEG and TETA (K1)</i>	11
3.1.2 <i>Part b: synthesis of CZTS NCs using OLA and 1-DDT (K2)</i>	11
3.1.3 <i>Optical microscopy</i>	12
3.1.4 <i>XRF and DLS</i>	13
3.1.5 <i>Post-annealing study based on XRD, Raman spectroscopy, SEM and UV-vis spectroscopy</i>	13
3.1.5.1 <i>TT0→TT1-(A) →TT2-(B)</i>	13
3.1.5.2 <i>TT0→TT1-(C) →TT2-(D)</i>	23
3.1.5.3 <i>TT0→TT1-(D) →TT2-(D)</i>	27
3.1.5.4 <i>TT0→TT1-(C)S</i>	32
3.1.6 <i>Carbon analysis</i>	34
3.1.7 <i>Resistivity</i>	35
4 KESTERITE POWDERS MADE BY HIGH-ENERGY BALL MILLING AS PRECURSORS OF SOLAR INKS.....	36
4.1 EXPERIMENTAL.....	36
4.2 RESULTS AND DISCUSSION.....	37
5 CONCLUSIONS.....	39
REFERENCES.....	41
ABBREVIAZIONI ED ACRONIMI.....	44

Sommario

La prima parte di questo rapporto riguarda la sintesi di nanocristalli di $\text{Cu}_2\text{ZnSnS}_4$ (CZTS) basata su oleilammina (OLA), con incorporazione di 1-dodecantiolo (1-DDT) attraverso il metodo di hot-injection (iniezione a caldo). L'1-DDT, usato come legante di coordinazione, è stato introdotto per migliorare, rispetto alle precedenti sintesi in OLA, la nucleazione e la crescita dei nanocristalli di CZTS. Le nostre osservazioni suggeriscono che l'uso di una quantità inferiore di OLA promuove una crescita omogenea dei grani nello strato assorbitore.

La diffrazione dei raggi X (XRD) ha rivelato polimorfi tetragonali ed esagonali della CZTS nei film ottenuti per spin coating prima dei trattamenti ad alta temperatura. In particolare, 1-DDT è responsabile della formazione di una maggiore percentuale della fase esagonale (del tipo ZnS-wurtzite) rispetto al caso in cui si usa solo OLA. In letteratura è riportato che la presenza di questa fase esagonale metastabile è utile per indurre una più efficace ricristallizzazione del materiale e ciò potrebbe spiegare la migliore morfologia dei film finali.

Bisogna però notare che il contenuto di carbonio dopo il trattamento termico finale è ancora abbastanza rilevante.

I trattamenti termici sono stati variati per ottenere non soltanto una buona cristallizzazione ma anche per minimizzare la presenza delle fasi spurie in maniera da avere la gap ottica tipica del CZTS (1.5 -1.6 eV) ed una resistività non troppo bassa. Per arrivare a questo risultato è stato effettuato uno studio comparativo tra post-ricottura con azoto, argon e vapore di zolfo in un forno tubolare. Le temperature dei due trattamenti termici (il primo TT1 senza zolfo ed il secondo TT2 con vapori di zolfo) sono state variate da 500°C a 600°C. Risultato di rilievo, abbiamo verificato la scomparsa nello spettro XRD di quasi tutti i riflessi delle fasi secondarie dopo la ricottura finale (TT2), a indicazione del loro sostanziale consumo nella formazione della fase CZTS. Tuttavia non essendo l'XRD da solo sufficiente per risolvere le diverse fasi, abbiamo effettuato ulteriori misurazioni di scattering Raman, che hanno rivelato invece in alcuni campioni, almeno in superficie, la presenza di fasi spurie binarie e ternarie anche dopo TT2. Questi campioni in effetti mostravano anche resistività e gap ottiche eccessivamente basse dimostrando l'utilità del Raman come tecnica di caratterizzazione. Le misure elettriche ed ottiche hanno anche mostrato la opportunità di non riscaldare troppo i campioni nel primo step in assenza di zolfo (TT1) per prevenire un loro probabile inizio di decomposizione.

Nella seconda parte del rapporto si descrive il lavoro svolto al fine di preparare le nanoparticelle di CZTS con un processo alternativo a costo ancora più basso della hot-injection: la macinazione ad alta energia. In queste prime prove le nanoparticelle sono state generate introducendo polveri dei quattro elementi puri dentro una giara in ottone e utilizzando 25 sfere dello stesso materiale. Come lubrificante è stato usato dell'etanolo. La durata della macinazione è stata nei diversi batch di 15, 30, 60, 90 e 180 minuti. Le particelle di CZTS si formano già dopo 15 min (insieme ai residui degli elementi e di altre fasi binarie e ternarie), e raggiungono quasi il 100% dopo 60 min (con un residuo di CuS di circa 1.5%) mentre sopra i 60 min appaiono delle contaminazioni dall'ottone delle sfere. Le particelle di CZTS generate in questo processo adottano una struttura cubica invece della struttura tetragonale di equilibrio probabilmente a causa della bassa temperatura del processo che inibisce un riordinamento dei cationi. Questo processo a basso costo per la produzione di "inchiostri solari" appare quindi promettente e si stanno considerando diverse modifiche per migliorarlo (ottimizzazione dei parametri di rotazione, utilizzo di giare e sfere in WC o zirconia per ridurre le contaminazioni, utilizzo di lubrificanti diversi che possano già fare parte dell'inchiostro finale).

1 Introduction

Despite of facing several challenges as photovoltaic absorber layer, kesterite (CZTS) structure based solar cells have successfully yielded efficiency beyond 10% [1]. For long term manufacturing developments, processing costs should be affordable and processing simple [2] [3], along the lines of the philosophy that for sustainability, cost effectiveness, high throughput, large production & promising conversion efficiency, non-vacuum based chemical methods are preferable [4] [5]. Annealing treatments have a major role in influencing the CZTS film properties. Therefore, deeper understanding of the impact of annealing parameters on the film formation and its properties is important for simplification and reliability of device fabrication [1]. Hence using suitable starting materials and design of successful annealing strategy is of primary interest.

2 Study on Synthesis and Post-annealing of $\text{Cu}_2\text{ZnSnS}_4$ Absorber Layers Based on Oleylamine/1-dodecanethiol

$\text{Cu}_2\text{ZnSnS}_4$ (CZTS) quaternary semiconductor nanocrystals (NCs) have been drawing significant research interest in the past few years as a promising active-layer semiconductor for low-cost thin-film solar cell application or thermal energy conversion to electricity [6] owing to its suitable optical properties, elemental availability, and non-toxicity of its constituents [7] [8] [9]. CZTS NCs have been mainly reported in two different crystallographic forms: tetragonal (kesterite) and hexagonal (wurtzite), the former being thermodynamically stable in ambient conditions [10]. One of the methods to obtain CZTS NCs with kesterite structure is high temperature synthesis with the use of simple metal salts in combination with elemental Sulphur using oleylamine (OLA) as solvent [11] [12].

The formation of a pure sulphide CZTS absorber layer with large grains has proved difficult so far. Based on our recent findings [11], the grain size is correlated with the amount and nature of organic residues, which in turns depend on the pyrolysis of OLA. However, the carbon residuals, especially those having long chains, cannot be fully eliminated by pyrolysis in inert atmosphere. In addition, OLA may also react with sulphur present in CZTS, forming a carbon layer with high resistance [6]. One way to optimize the CZTS NCs is to replace OLA with other solvents that form less stable complexes with metallic cations which, possibly, can also be easily removable during annealing at high temperature. In this work, CZTS NCs were synthesized from metal chlorides, as inexpensive and non-toxic starting materials, with two different strategies:

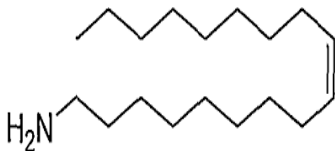
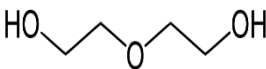
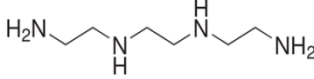
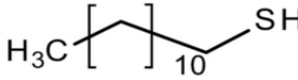
1. use of short-chained organic materials, such as diethylene glycol (DEG) and triethylenetetramine (TETA) instead of oleylamine (OLA);
2. a mixture of oleylamine (OLA) and 1-dodecanethiol (1-DDT) to reduce the amount of OLA;

The chemical structures and the function of OLA, DEG, TETA and 1-DDT in the synthesis are shown in Table 1.

According to literature [12], 1-DDT can act as a coordinating agent to produce complexes with the metal cations (Cu, Zn, and Sn) and control the reactivity of different cations in the reaction solution. These complexes would decompose into corresponding sulphides at a certain temperature condition. During the formation of CZTS nanocrystals, 1-DDT plays an important role in the process of determination of the CZTS nanocrystals shape and grain size. In addition, 1-DDT acts as an additional sulphur source in the synthesis of CZTS nanoparticles [13]. 1-DDT has the tendency to slow the release of sulphur atoms as it undergoes

decomposition at high temperatures. Furthermore, the thiol group in 1-DDT can quench the band gap emissions in CdS=ZnS core-shell nanostructures [14].

Table 1 The chemical structures and the properties of OLA, DEG, TETA and 1-DDT

Reagents	Structure	Boiling point [°C]
OLA		364
DEG		244
TETA		266.6
1-DDT		275

This work aims to provide an account of the use of ligand-free DEG and TETA, and a hybrid of OLA and 1-DDT in synthesis of CZTS NCs using the hot-injection technique; this step of production of an 'ink' is followed by spin coating and then annealing of the deposited layers. In addition, the effect of different annealing atmospheres (N₂, Ar and sulphur) on the grain dimension in final thin films is discussed. The elemental composition and size, structural, optical, morphological and electrical properties of CZTS thin films have been investigated by X-ray fluorescence (XRF) analysis, Elemental analysis, Glow Discharge Optical Emission Spectroscopy (GDOES), Dynamic Light Scattering (DLS), X-ray diffraction (XRD), Raman spectroscopy, UV-vis spectrometry, Scanning Electron Microscopy (SEM) and 4-point probe resistivity measurement.

2.1 Experimental part

Copper (II) chloride di-hydrate ($\text{CuCl}_2 \cdot 2\text{H}_2\text{O}$, Aldrich >99%), Zinc chloride anhydrous (ZnCl_2 , Alfa Aesar >98%), Tin (II) chloride di-hydrate ($\text{SnCl}_2 \cdot 2\text{H}_2\text{O}$, Alfa Aesar 98%) were dehydrated for 1 hour and kept under vacuum. Sulphur (S, Aldrich >99.5%), Oleylamine (OLA, Aldrich, 70%), Diethylene glycol (DEG, Aldrich, 99%), Triethylenetetramine (TETA, Aldrich, >97%), 1-Dodecanethiol (1-DDT, Aldrich, 90%), Toluene (Aldrich, >99.7%) and Ethanol (VWR chemicals, >99%) were used without further purification.

2.1.1 Synthesis of CZTS NCs using DEG and TETA (K1)

According to the work of Mirbagheri et al. (2016) [15], 2 mmol of CuCl_2 , 1.50 mmol of ZnCl_2 and 1.09 mmol of SnCl_2 are mixed with 7 ml DEG in a round-bottom flask equipped with a reflux condenser. The reaction mixture was degassed for 20 min under stirring at room temperature, and then the temperature was increased to 220°C while purging with nitrogen. Afterwards, a solution containing 5.60 mmol of S, 2 ml DEG and 2 ml TETA was quickly injected to the flask while stirring the solution. Then the mixture was kept under stirring at 220°C for 2 hours, and thereafter the resulting mixture was allowed to naturally cool down to room temperature.

The final suspension was treated with a solution of toluene:ethanol=1:5 (V/V) and centrifuged for 10 minutes at 4000 rpm in order to separate the solvent from the CZTS nanoparticles. The obtained product (K1) is about 1.5 g. Toluene was finally added to obtain an ink with viscosity suitable for deposition of thin films by spin-coating. The scheme of the synthesis is shown in Figure 1.

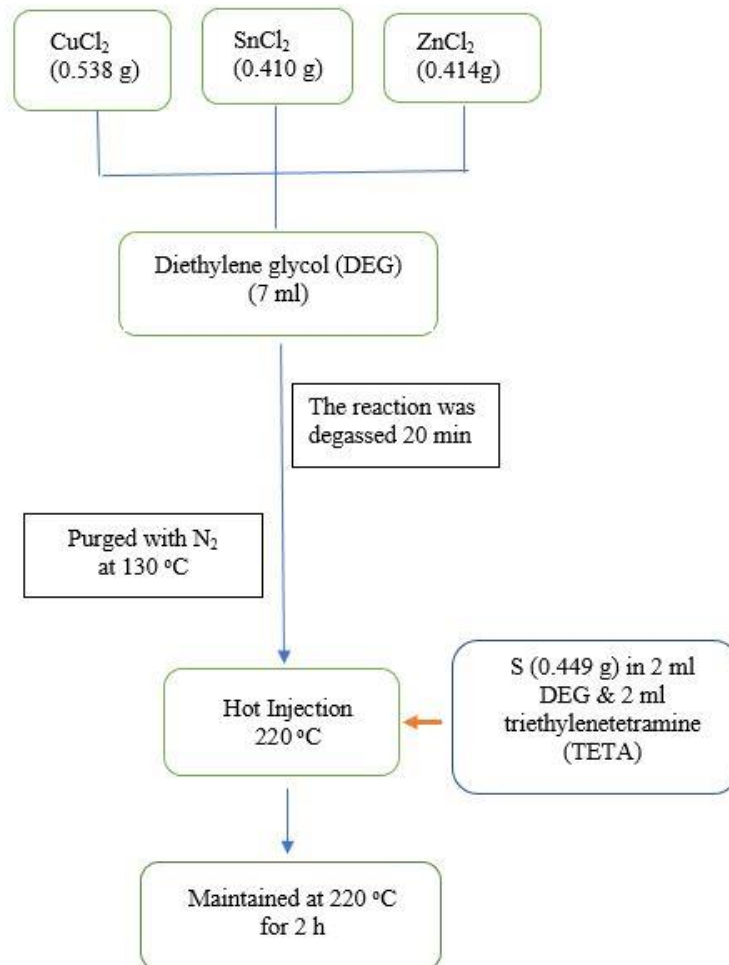


Figure 1 Scheme of the principal steps to synthesize the CZTS nanoparticles (K1) using DEG and TETA

2.1.2 Synthesis of CZTS NCs using OLA-1-DDT (K2)

In a standard synthesis, as shown in Figure 2, 2 mmol of CuCl_2 , 1.5 mmol of ZnCl_2 and 1.09 mmol of SnCl_2 are dissolved in 6.6 ml oleylamine into a 100 ml three-neck round bottom flask. The round bottom flask is then placed on a hotplate stirrer. All the experiments were carried out in a standard air-free condition using a Schlenk line apparatus. The mixture was degassed at 130°C . In the meantime, sulphur powder (5.6 mmol) and 1-DDT (5 ml) were dissolved in OLA (3 ml). The sulphur-OLA-DDT solution was rapidly injected in the hot solution at 270°C under N_2 flux. The mixture was kept at that temperature for 30 minutes and then cooled at room temperature. The final suspension was treated with a solution of toluene:ethanol=1:5 (V/V) and centrifuged for 10 minutes at 4000 rpm in order to separate the solvent from the CZTS nanoparticles. The obtained product (K2) is about 1.5 g. Toluene was finally added to obtain an ink with viscosity suitable for deposition of thin films by spin-coating.

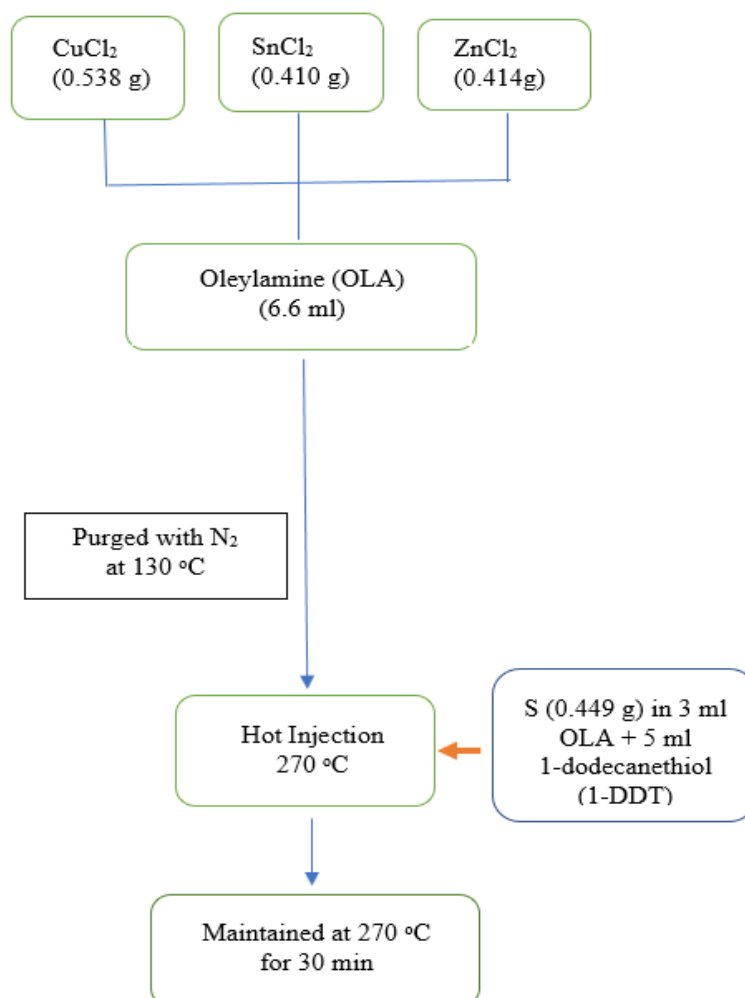


Figure 2 Scheme of the principal steps to synthesize the CZTS nanoparticles (K2) using OLA and 1-DDT

2.1.3 Thin film deposition

Substrates were Soda Lime glass (SLG) with dimension of 2x2 cm². They were kept in ethanol and sonicated for 30 minutes, then washed with distilled water and ethanol, and dried with argon gas.

The CZTS nanoparticles were dispersed in toluene and ultra-sonicated until a homogeneous ink was obtained. The ink was then deposited on SLG substrates by spin-coating. Deposition parameters of 60μl at 1200 rpm for 30 seconds were applied to obtain CZTS film.

After the film deposition, residual toluene was removed with a soft thermal treatment (TT0) using a hot-plate. The temperature for soft thermal treatment (TT0) is also manipulated to observe its effect on the film surface. Different temperature of 150°C and 200°C with different thermal treatment time of 10 min and 15 min were used for the absorber layer, aiming at the production of crack-free films. The samples were cooled down naturally to room temperature before further analyses.

Thermal treatments (TT) at high temperature were performed in a tubular furnace to promote the grain growth. They consist of a two-step thermal annealing in different inert atmosphere (N₂, Ar), TT1 and TT2, respectively. During the TT2 thermal annealing sulphur vapour is provided. The temperature profiles (A, B, C and D) for TT1 and TT2 are shown in Figure 3.

In a previous work [11], the condition A and B have been used for TT1 and TT2, respectively. Anyway, the high heating rate (20°C/min) has caused cracks, poor adhesion and overall quality of the films. Thus, after some testing, the heating rate was decreased to 3°C/min (Figure 3 C-D). This proved as a rather important change in our production protocols.

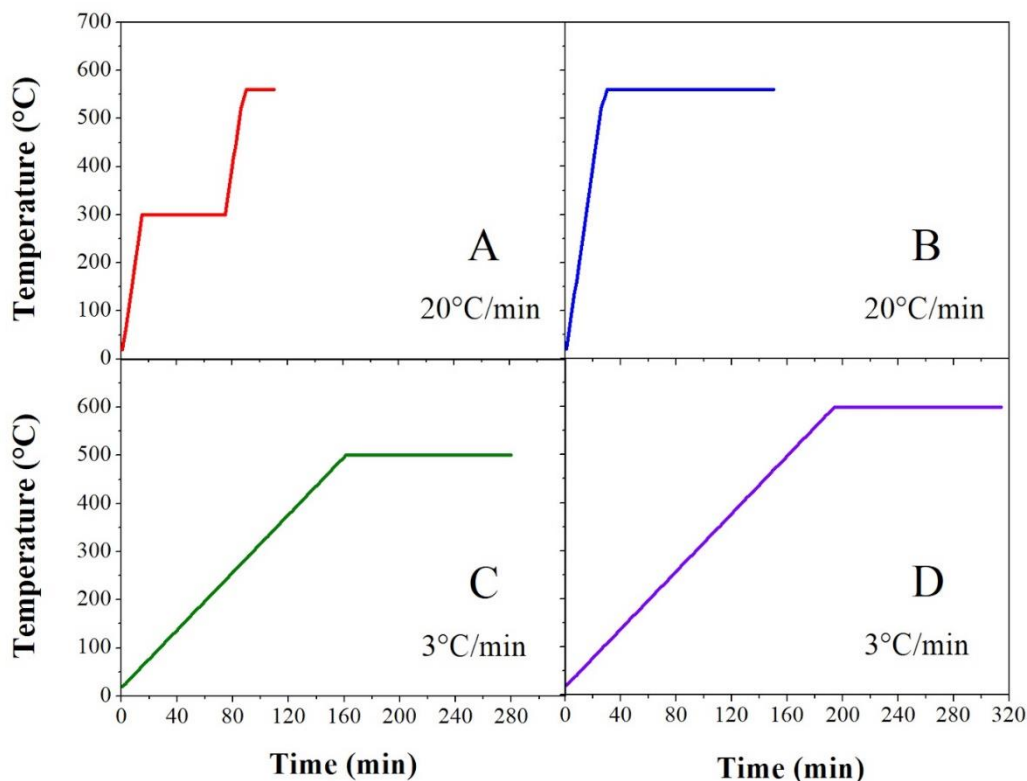


Figure 3 Heating ramps of thermal treatments for TT1 and TT2

2.1.4 NCs and thin films characterization

The elemental composition of the synthesized CZTS nanocrystals was determined by XRF. An ARL X'TRA, Thermo Fisher scientific instrument was used for measurements performed on as-spun films, treated only with the soft annealing TT0. A CHN analysis was performed with a LECO elemental analyser to determine the absolute carbon concentration. The analysis is based on a rapid and complete combustion (Flash) of the sample at 950°C and in excess of oxygen. The combustion products are then passed through a second furnace (Afterburner) at 850°C for further oxidation. The gases are then collected in a container inside which they are homogenized and sent to the infrared absorption detectors for the measurement of Carbon in the form of CO₂.

Glow Discharge Optical Emission Spectroscopy (GDOES) was used to analyse the depth profiles of the CZTS elements and to detect possible organic residuals in the material by monitoring the carbon signal with a GD-Profilier 2 – Horiba Jobin-Ivon instrument. In fact, differently from the chemical characterization techniques commonly used such as EDX or XRF, GDOES allows the identification of light elements, like carbon, of interest in this work to study the organic residuals in different CZTS films grown from NCs inks.

Structural information on NCs was obtained by XRD using a Panalytical X'Pert MRD instrument equipped with CoK α sealed tube operated at 40 kV, 40 mA. The XRD pattern was analysed with Jade Version 6 software.

The hydrodynamic size of NCs was characterized by DLS using a Delsa Nano C (Beckman Coulter). DLS measures the intensity of the laser light scattered from suspended particles. The dispersion hydrodynamic diameter is derived from the temporal evolution of the scattered light intensity using the Stokes-Einstein equation. In all the experiments, the nanoparticle dispersions were sonicated for 15 min using an ultrasonic bath (40 W, 35 kHz, Elma 460/H) before the size and zeta potential measurement. All the measurements were carried out at 25°C. The reliability of the hydrodynamic size values was verified with more than 10 measurements for each analysis.

An optical microscope (HX -1000™ by Remet) was used to observe the surface morphology of the films after TT0. SEM analysis was performed using a JEOL JSM-7001F Field Emission SEM equipped with an Oxford INCA PentaFETX3 Energy Dispersive X-ray Spectroscopy (EDXS) detector. In addition, some of the SEM analysis were performed using a COXEM EM-30AX SEM and A Jeol JMS 7401F Field-Emission SEM.

The optical properties of CZTS NCs were investigated on thin films deposited on SLG substrates by spin coating after the different thermal treatments (TT0, TT1 and TT2), using a spectrophotometer produced by Perkin-Elmer, model LAMBDA 950, equipped with a 150mm integrating sphere. The normal incidence transmittance (T) and reflectance (R) were measured and the absorption coefficient (α) was estimated using the approximated equation:

$$\alpha = -\frac{1}{d} \cdot \ln \left(\frac{T}{1-R} \right) \quad (1)$$

where d is the film thickness, measured with a stylus profilometer, or evaluated from the SEM cross section images. The bandgap energy was obtained by a linear fit of $(\alpha E)^2$ versus E (Tauc's plot), as used for direct bandgap semiconductors.

Raman spectra were collected using a LabRAM Aramis (Horiba Jobin-Yvon) equipped with an optical microscope and a 100 \times objective. A diode-pumped solid-state laser source of 532 nm was used for the excitation of the Raman signal that was detected with an air-cooled charge-coupled device. The slit width of the spectrometer was typically set at 100 μ m. A diffraction grating with 1800 lines mm⁻¹ was used for the collection of all Raman spectra with an overall spectral resolution of \sim 1 cm⁻¹. Raman spectra have been acquired with an overall acquisition time of 10 s by setting the laser power at 0.02 mW.

The sheet resistance was performed by S-302 Resistivity Stand (Four points probe apparatus).

3.1 Results and discussion

3.1.1 Part a: synthesis of CZTS NCs using DEG and TETA (K1)

The K1 synthesis using DEG and TETA exhibits poor adhesion to the substrates, as shown in Figure 4. This indicates that as the solvents and organics are removed, tensile stress builds up in the film, resulting in cracking and inhomogeneity [5]. In fact, SEM micrograph shows a phase separation and incompatibility of DEG and TETA with other reagents used in the synthesis.

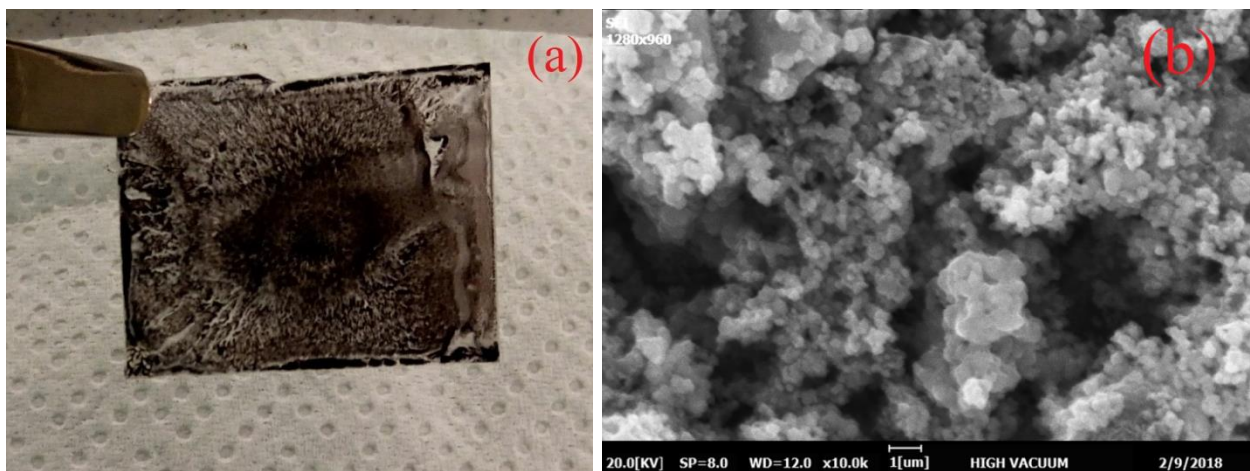


Figure 4 a) Photo of as-deposited and b) SEM image of CZTS film using DEG and TETA on SLG substrate (TT0)

Film formation is dependent on solution concentration and viscosity. In addition, adhesion is one of the important parameters for the correct functioning of the cell, along with homogeneity of the absorber layer. Furthermore, deposited layers must be “crack-free”, as cracks may lead to short-circuit formation. Several attempts have been done in order to improve the adhesion of the ink to SLG substrates, including:

- use of different washing steps (different volume ratio of ethanol and toluene);
- use of different solvent (ethanolamine, chloroform, isopropanol);
- use of binder (ethylene glycol);
- use of different substrates (silicon, molybdenum coated SLG, SLG treated with HCl).

For all the above attempts, after the soft thermal treatment (TT0) the film turned into powder, losing its adhesion properties. The above observations confirmed the importance of oleylamine, which acts as strong chelating agent and, at the same time, capping agent on the surface of the CZTS nanoparticles, thus improving adhesion.

3.1.2 Part b: synthesis of CZTS NCs using OLA and 1-DDT (K2)

At least a low amount of OLA is necessary to obtain CZTS films of good morphological quality. Accordingly, OLA mixed with 1-dodecanethiol (1-DDT) was tested as solvent, in order to modify the carbon residuals in the final CZTS films, favoring the growth of larger crystals, without detriment to their adhesion to the substrate. As visible in Figure 5, the spin-coated samples made with the ink containing OLA and 1-DDT appear homogeneous and well adhering to SLG substrate.

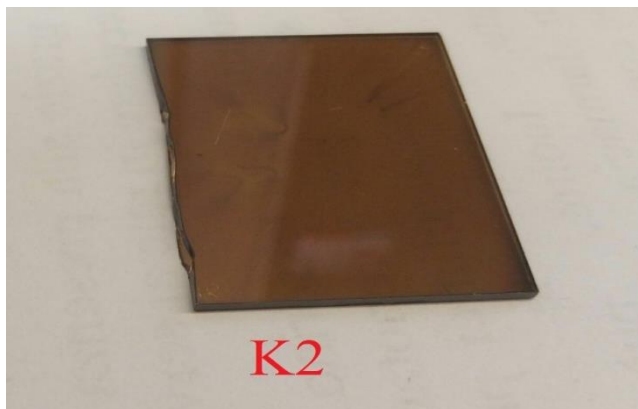


Figure 5 Photo of as-deposited CZTS nanoparticles using OLA and 1-DDT on SLG substrate

3.1.3 Optical microscopy

The presence of cracks in CZTS films can be easily observed by optical microscopy. Figure 6 shows the surface morphology of CZTS films with the thickness of $\sim 1.5 \mu\text{m}$ required for the absorber layers. In order to obtain crack-free films, TTO was tested at two different temperatures of 150 and 200°C, with annealing times of 10 or 15 min. All samples annealed at 200°C show cracks, whereas, the sample annealed at 150°C is crack-free. In addition, by increasing the time of annealing the spots, which represent the agglomeration on the surface of the films, are decreased. Based on this result, samples annealed at 150°C for 15 min were used for further analysis. Both the loss of solvent and the thermal expansion mismatch between film and substrate can cause crack formation. The first effect is minimized by applying multiple thin films, annealing each one after deposition. The second can be handled, although not completely eliminated, if film thickness is limited. As a rule of thumb, a film thicker than $0.5 \mu\text{m}$ cracks, unless it is well adherent to the substrate.

However, in our attempts we could not obtain high-quality films by depositing multiple thin layers.

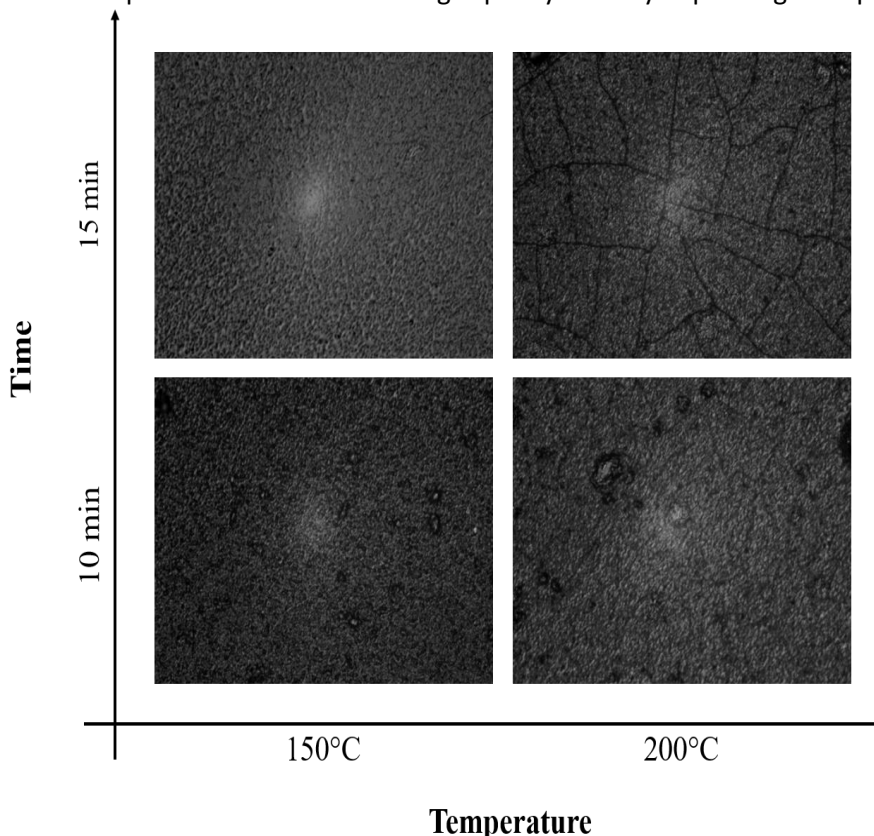


Figure 6 Optical microscopy of K2 film with $\sim 1.5 \mu\text{m}$ thickness after TTO treatment

3.1.4 XRF and DLS

Table 2 shows the chemical composition and particle size of K1 and K2 synthesis. All elements are uniformly distributed and the final composition of K1 and K2 is the desired one. In fact, there is no significant loss of any elements, and their ratios are close to the values expected for high-performance solar cell applications. This can also confirm that CZTS nanocrystals have been formed. DLS measurements carried out on the precursor ink show that the average dimension is around 20 nm.

Table 2 The relative concentration of metals (normalized to Cu=2) and DLS data of K1 and K2 synthesis.

Sample	XRF (assuming S=4)					Cumulant size (nm)	PI	Note
	Cu	Zn	Sn	Cu/Sn	Zn/Sn			
Ideal composition	1.81	1.21	0.98	1.75-1.9	1.2			
K1 (DEG+TETA)	1.83	1.23	0.94	1.94	1.31	21.2	0.03	Monodisperse
K2 (OLA+1-DDT)	1.79	1.20	1.01	1.78	1.20	24.1	0.05	Monodisperse

3.1.5 Post-annealing study based on XRD, Raman spectroscopy, SEM and UV-vis spectroscopy

3.1.5.1 TT0→TT1-(A) →TT2-(B)

XRD analysis was performed on the samples of K2 deposited on SLG substrates under different thermal treatment (TT0, TT1 and TT2) using different atmosphere (N₂, Ar and sulphur (S)).

As can be seen in Figure 7a, two phases are identified in TT0; tetragonal CZTS (PDF#26-0575) and hexagonal (ZnS-wurtzite type) (PDF#75-1547) CZTS. The peaks at $2\theta = 21^\circ, 33^\circ, 38^\circ, 55^\circ, 66^\circ$ and 82° were attributed to the diffraction of (1 0 1), (1 1 2), (2 0 0), (2 2 0), (3 1 2) and (0 0 8) tetragonal kesterite, respectively. The peaks at $2\theta = 31^\circ, 33^\circ$ and 35° correspond to (1 0 0), (0 0 2) and (1 0 1) planes, respectively, in the hexagonal phase. The formation of a wurtzite phase could be due to using 1-dodecanethiol in the synthesis. The covalently bonded S in 1-DDT is very stable and hence difficult to be broken down to release the S atom for the reaction, resulting in a slow reaction rate, a condition that concurs to the formation of the wurtzite phase. In addition, a copper sulphide (Cu₂S) peak is observed at $2\theta = 37^\circ$ (PDF#65-2980).

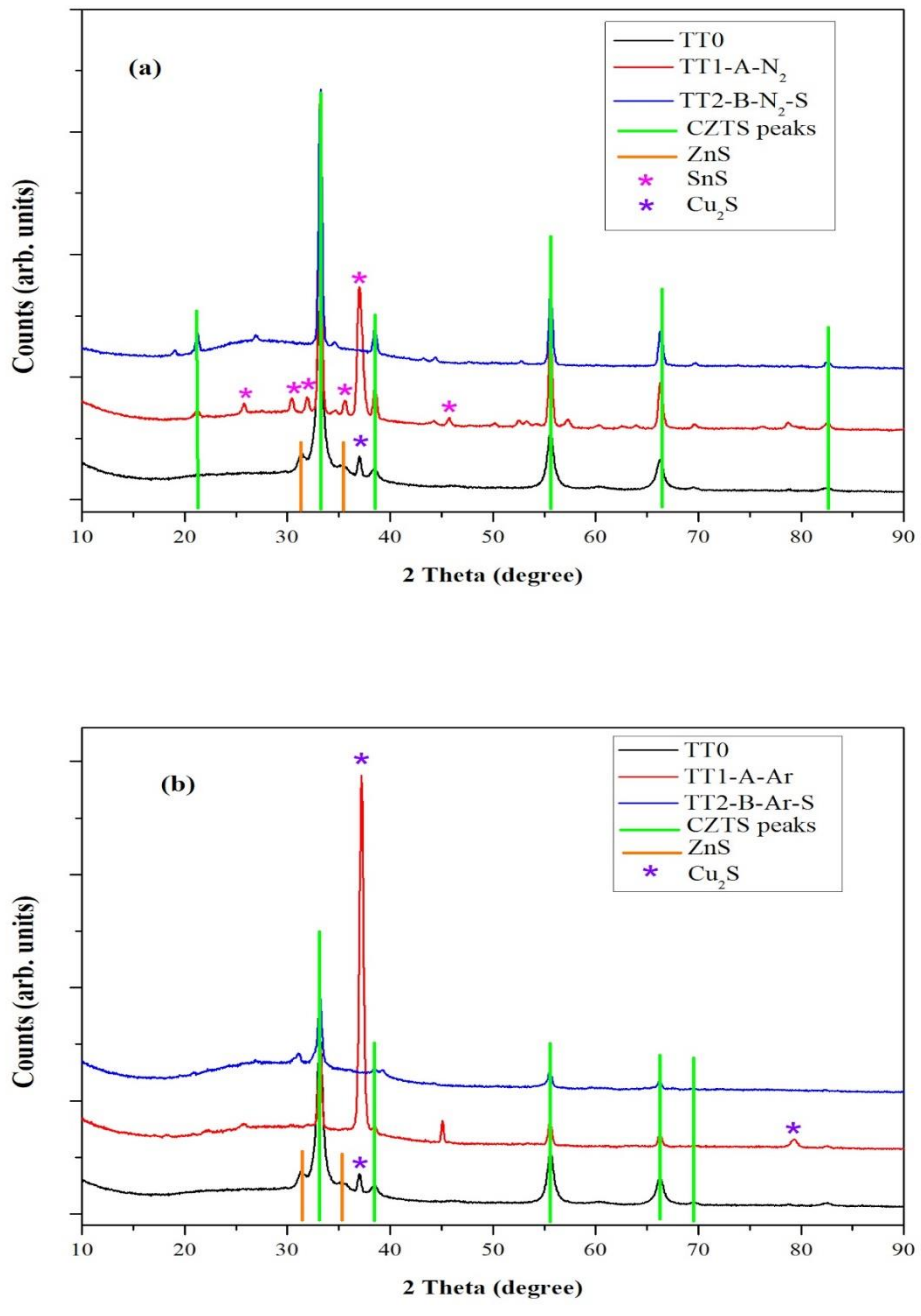


Figure 7 XRD spectra of K2 sample at different thermal treatments (TT0, TT1 and TT2) under: a) N₂ b) Ar atmosphere

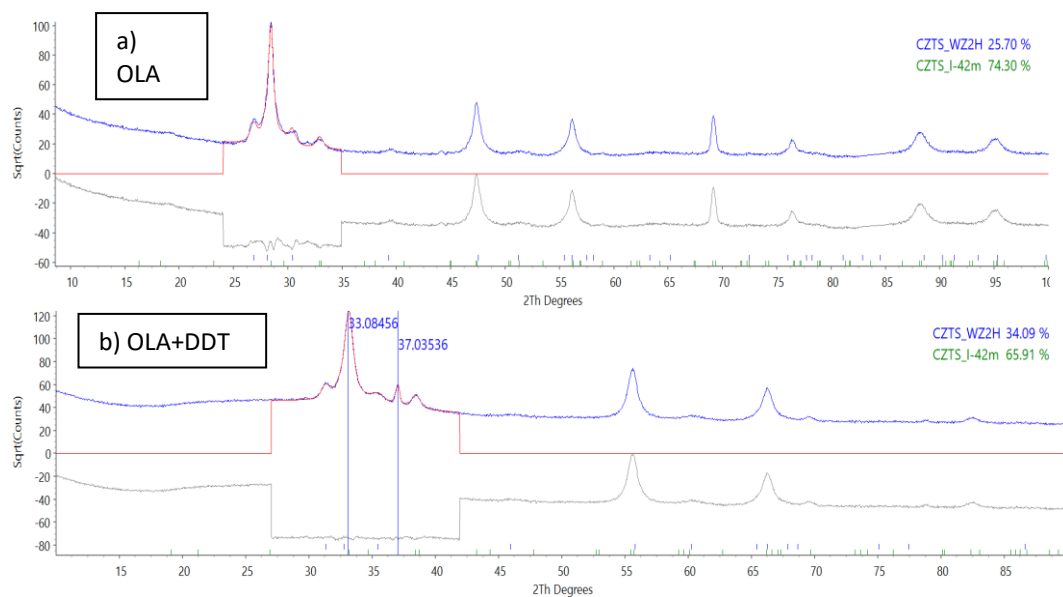


Figure 8 XRD spectra of samples a) OLA (data collected with $\text{CuK}\alpha$ radiation), b) OLA+DDT (data collected with $\text{CoK}\alpha$ radiation) at TT0 analyzed by Topas

The comparison between XRD pattern of samples OLA [11] and OLA+DDT at TT0 analyzed by Topas is shown Figure 8. For the OLA/DDT sample two additional features indicated by the two blue bars have to be introduced: the broad halo of amorphous glass substrate near the CZTS peak at about 33° ; (ii) the peak at 37° assigned to $\text{Cu}_2\text{-xS}$. In our previous results, with the preparation based on OLA only [11] the hexagonal fraction was about 20% which is apparently less than in the OLA/DDT sample. It seems that OLA/DDT produced a larger amount of hexagonal phase: the peaks are broader with OLA/DDT, that is, smaller nanocrystalline domains. Actually, the smaller size might be the reason for the higher amount of hexagonal with respect to the previous preparation with OLA only.

After TT1 (560°C with a heating rate of $20^\circ\text{C}/\text{min}$) in N_2 atmosphere (Figure 7a) the peaks of kesterite become sharper, as a consequence of crystal growth. In addition, the spurious phase, copper sulphide, disappears while tin sulphide (SnS) is detected (PDF#39-0354). Different temperatures tend to stabilize different phases. In fact, after the second thermal treatment (TT2), where sulphur vapour is present during the treatment, the secondary phases disappear, indicating that tin sulphide takes part in the formation of the CZTS nanocrystals.

Figure 7b shows the XRD pattern of samples annealed in Ar atmosphere. Thermal treatment (TT1) leads to an increase of crystal size, and the intense peak at $2\theta=37^\circ$ suggests the presence of copper sulphide (Cu_2S) (PDF#72-1071). A possible occurrence of extra phases, mainly pure or mixed copper sulphides in the production of kesterite films, has already been reported in the literature [16] [17]. It was found that the spurious phase disappears after TT2, indicating that thermal treatment in sulphur atmosphere improves the stability condition of CZTS.

Our observations indicate that at 560°C , the secondary phase of SnS tends to appear after TT1 under N_2 gas, whereas Cu_2S tends to appear under Ar atmosphere. In both conditions, by introducing sulphur vapour in the treatment atmosphere leads to disappearance of all impurities, thus making the CZTS crystal structure stable.

Evidence provided by XRD is not conclusive on phase identification: purity of the CZTS nanocrystals cannot be assessed. Raman spectroscopy was used to complement the XRD analysis as it can give a better indication of the presence of secondary phases; in fact, each phase among those involved in this work give a peak position in Raman scattering which in some cases is more distinct than in the corresponding XRD patterns. Raman spectroscopy can detect secondary phases such as Cu_xS , ZnS , Cu_2SnS_3 , and others.

Therefore, the as-synthesized CZTS nanocrystals (TT0) and annealed samples (TT1) were examined by Raman spectroscopy.

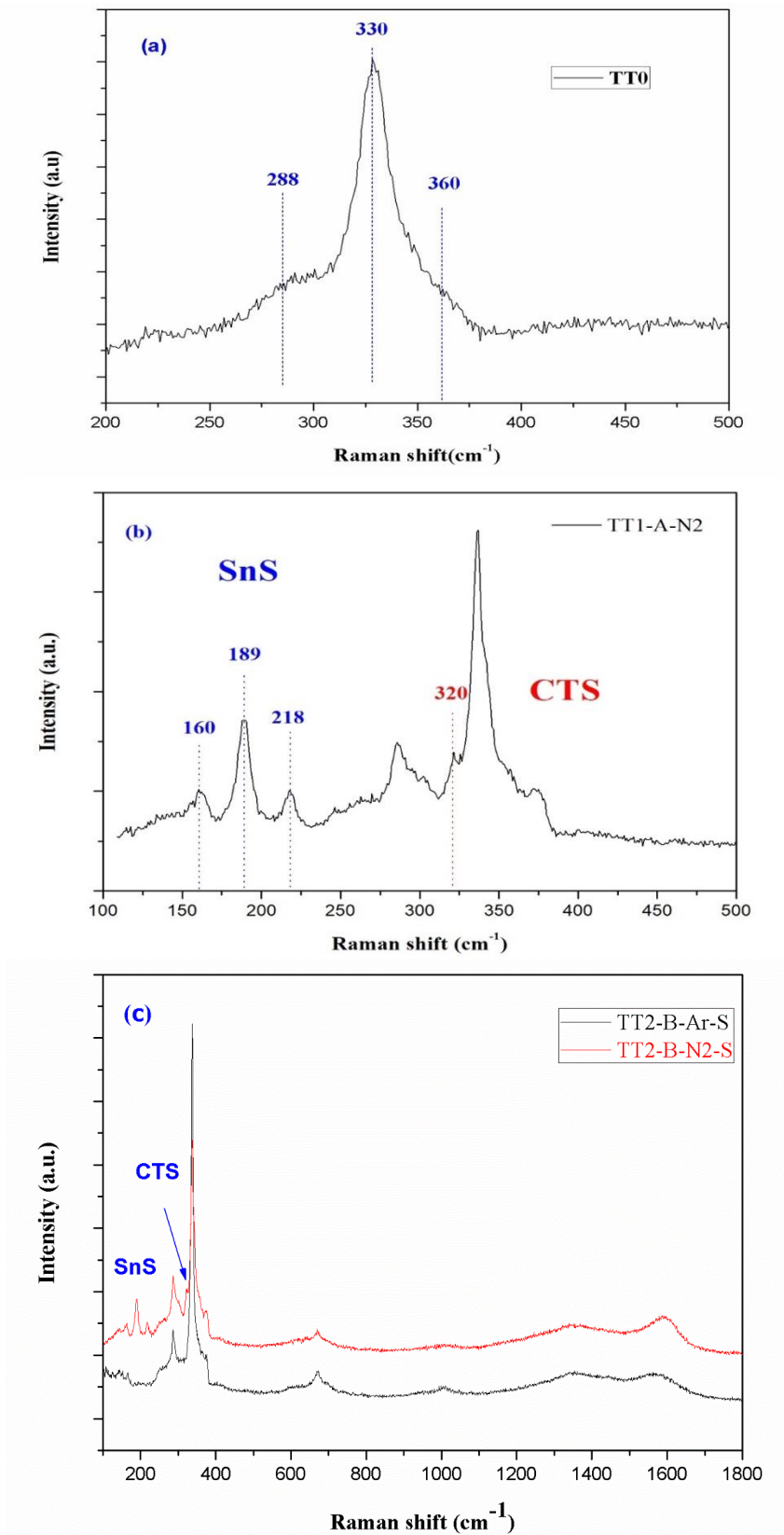


Figure 9 Raman spectra of sample a) TT0 b) TT1-A-N₂ c) TT2-B-Ar-S and TT2-B-N₂-S

Figure 9a shows the Raman spectra of CZTS thin film after TT0. Raman spectrum shifts of CZTS are shown at 288, 330 and 360 cm^{-1} respectively [18]. The stronger peaks at 330 cm^{-1} is due to the A_1 symmetry and it is related to the vibration of the S atoms in CZTS [19] [20]. Peaks at 288 cm^{-1} are attributed to the vibration of the Zn atoms and S atoms with some contribution from the Cu atoms in CZTS lattice [20]. The secondary phase Cu_2S , observed in the XRD pattern (Figure 7) is not observed in the Raman spectra, a feature made evident by the absence of peaks at 475 cm^{-1} [21]. This suggests that Cu_2S could be in the bulk of the film, seen by XRD but not easily reached by Raman. The Raman scattering spectra of the sample after TT1 (Figure 9b) shows three peaks at 160 cm^{-1} , 189 cm^{-1} and 218 cm^{-1} , corresponding to the SnS phase [22], in agreement with the XRD data (Figure 9a). In addition, the left shoulder on the larger CZTS peak at 320 cm^{-1} is likely due to Cu_3SnS_4 [22] which cannot be distinguished from CZTS in the XRD pattern. SnS and Cu_3SnS_4 phases remained unaffected after TT2 under nitrogen. Whereas, these phases cannot be seen in sample treated under argon atmosphere (TT2-B-Ar-S) as shown in Figure 9c. In addition, in both samples we could observe the peak corresponded to carbon which normally appear at wavenumber of 1800-1000 cm^{-1} .

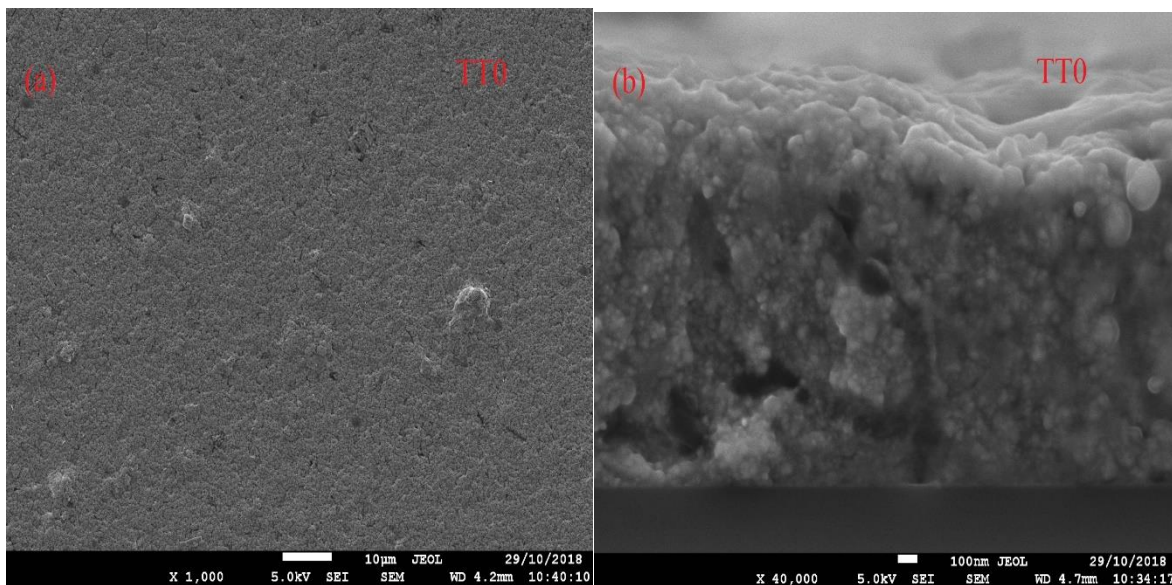


Figure 10 SEM image of CZTS thin film after TT0: a) planar, b) cross section

Figure 10 (a-b) shows the SEM images of the surface and cross-section, respectively, of a CZTS film after soft thermal treatment (TT0). The surface appears uniform and without cracks. The cross-section image reveals the compact morphology.

Figure 11 (a-d) shows the SEM images of the surface and cross-section, respectively, of a CZTS film after TT1 in N_2 atmosphere. Grains appear to be grown compared to those in Figure 10b. Moreover, some “Feathers like” impurities of copper tin sulphide (CTS), as confirmed by EDX analysis, were formed on the surface of the films (Figure 11 b-d). The presence of CTS is also revealed by the peak at 320 cm^{-1} in the Raman spectrum.

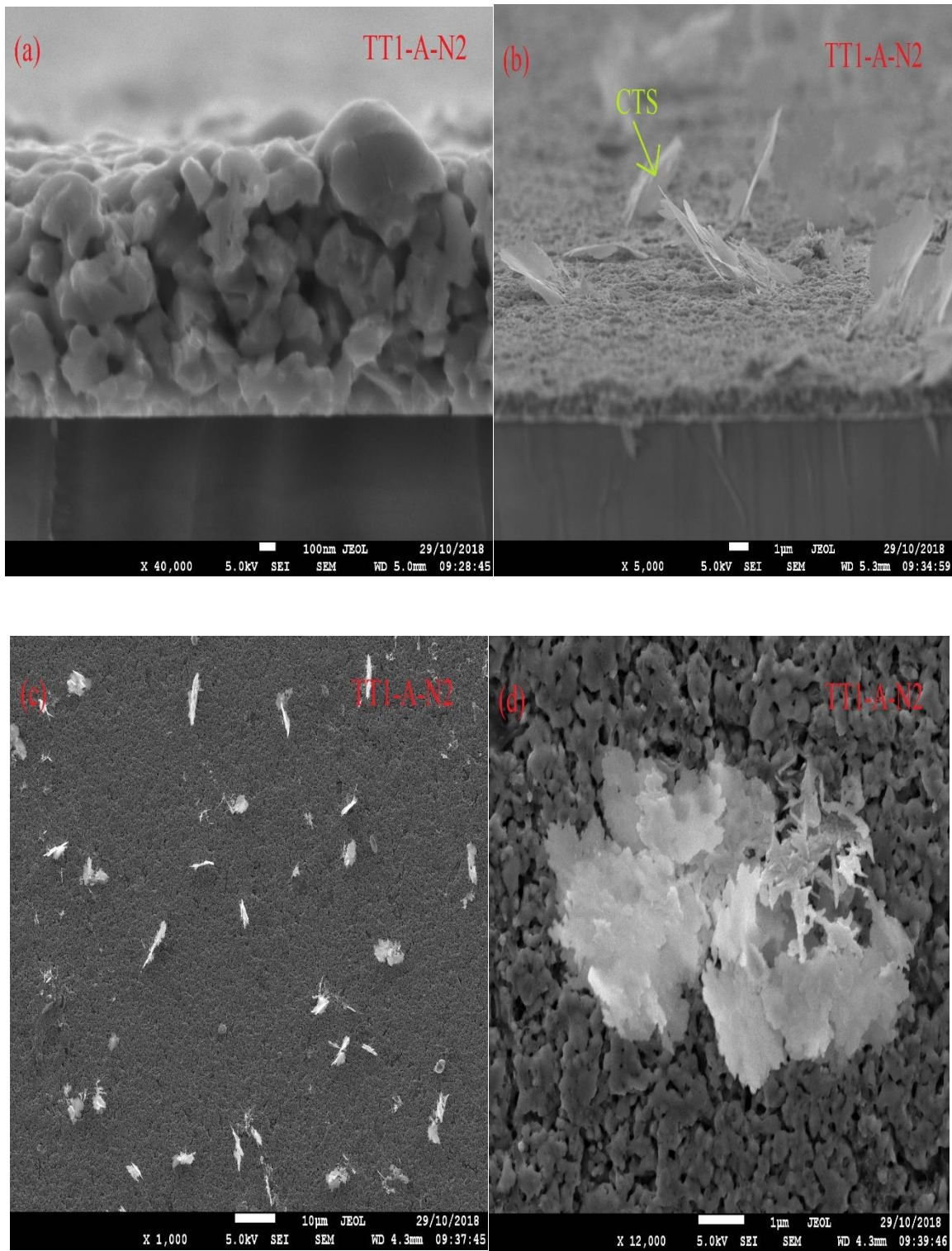


Figure 11 SEM image of CZTS thin film after TT1 under N₂ atmosphere: a,b) cross section; c,d) planar.

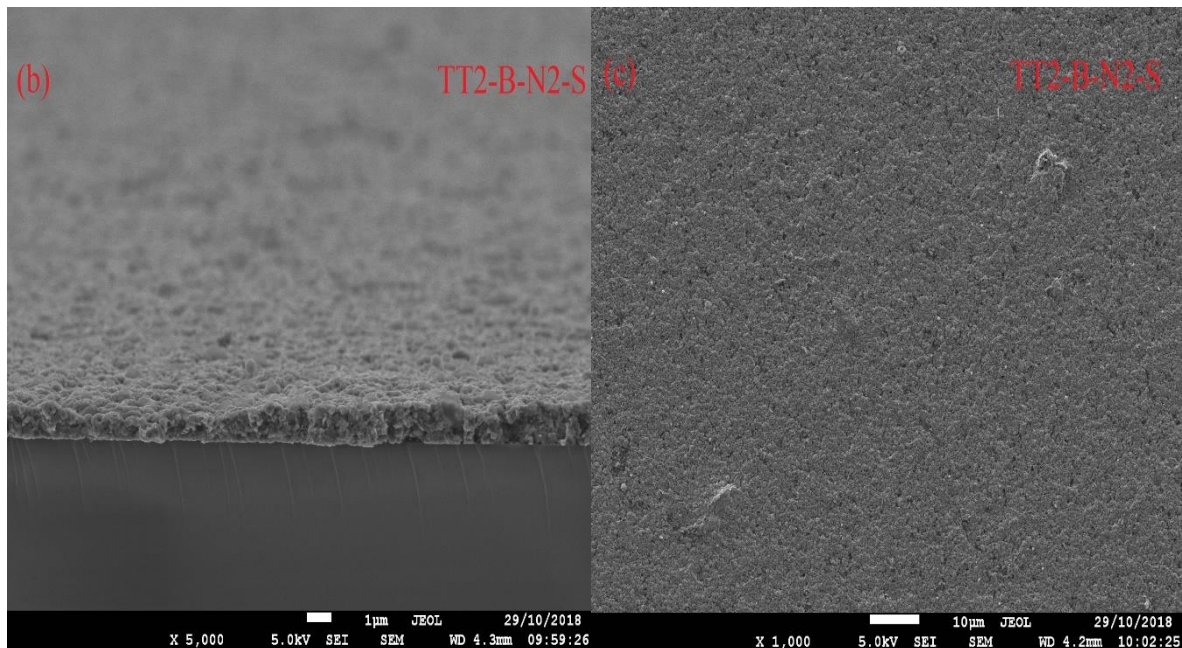
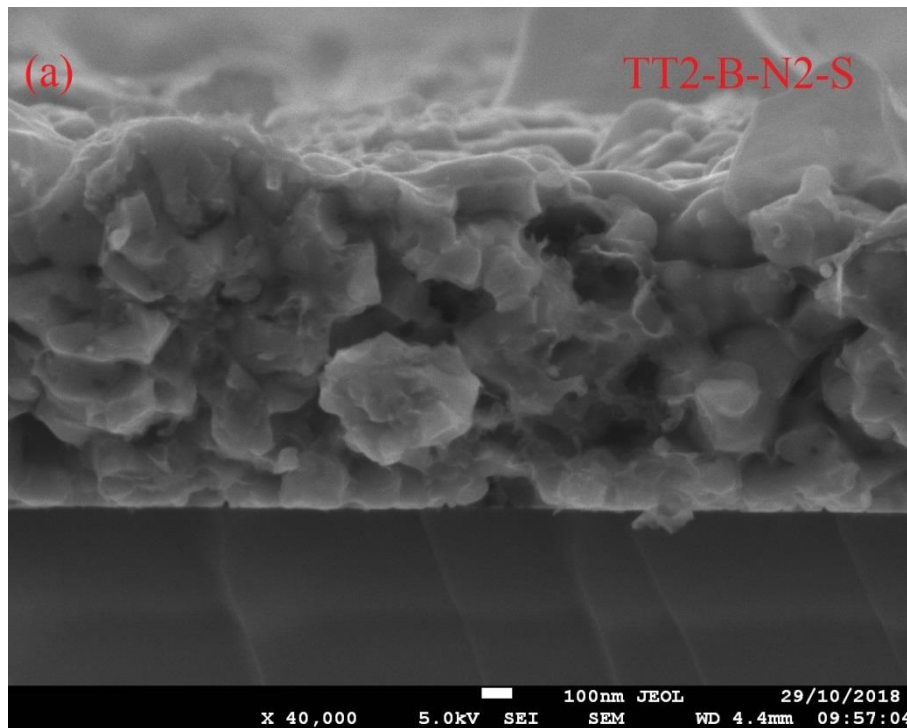


Figure 12 SEM image of CZTS thin film after TT2 under N₂ atmosphere: a,b) cross section; c) planar.

Figure 12a shows the SEM images of the surface and cross-section of the film after TT2 in N₂ atmosphere together with sulphur vapour: it can be clearly seen that the grain size increased thanks to the presence of the sulphur vapour. In addition, the feather-like features (CTS) disappeared (Figure 12 b, c), confirming that the Sulphur atmosphere is essential to improve crystal growth and eliminate spurious phases, stabilizing the CZTS phase. The SEM results are in good agreement with the corresponding XRD data.

The cross-sectional SEM images of annealed CZTS films under Ar atmosphere, without and with S vapor are shown in Figure 13 a and b, respectively. The microstructure of the first film consists of a mixture of small nanocrystals randomly distributed among large nanocrystals (70-150 nm). In Figure 13b, it can be observed large grains (500 nm), demonstrating that the annealing in Sulphur vapor favors the grain growth. This tendency is in good agreement with the results of the XRD analysis.

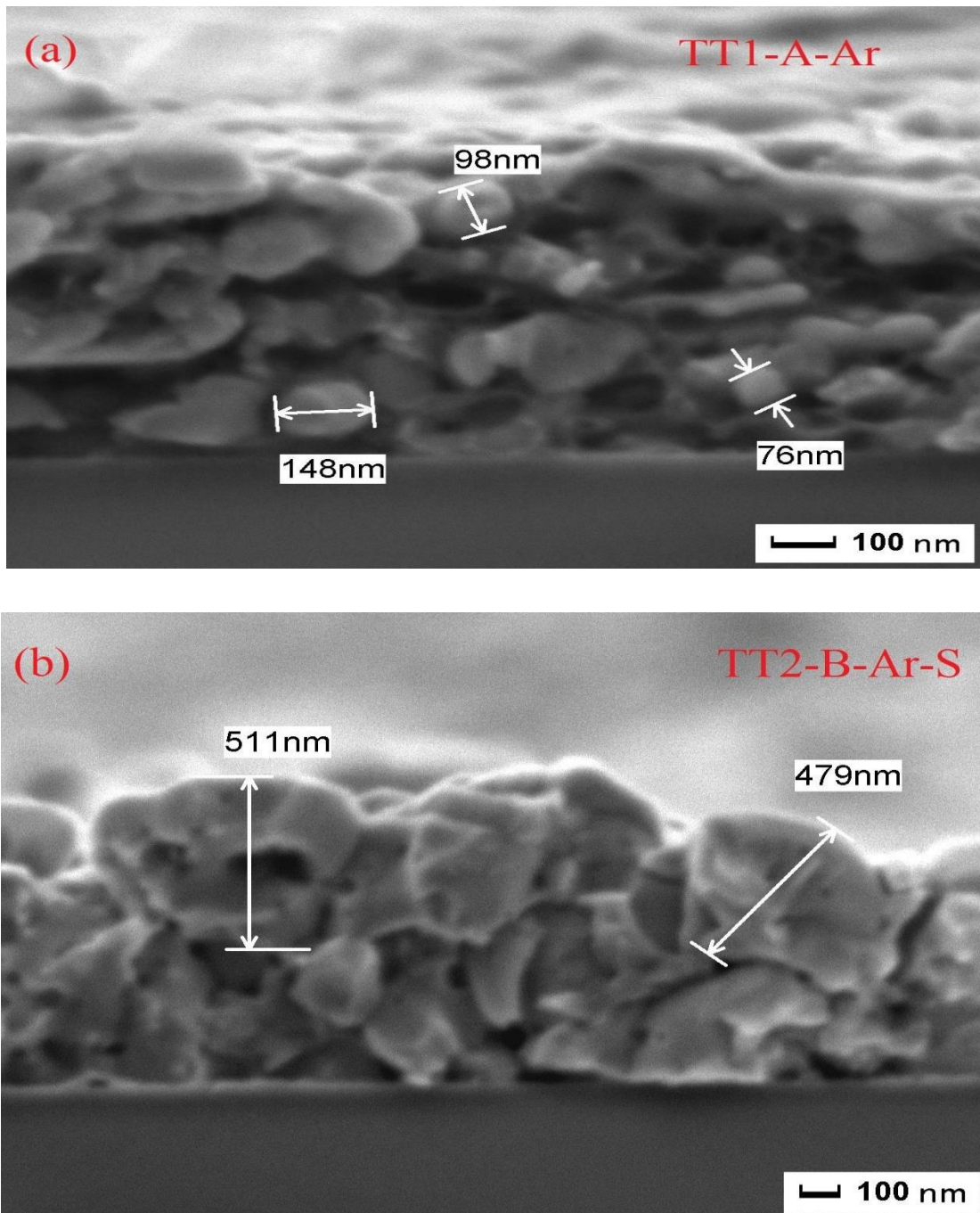


Figure 13 SEM image of CZTS thin film under Ar atmosphere: a) TT1-A-Ar; b) TT2-B-Ar-S

Figure 14 shows the transmittance spectra of CZTS films after TT0, TT1 at 560°C, and TT2 at 560°C with S, under N₂ atmosphere (a), and Ar atmosphere (b). In the same figure also the corresponding $(E\alpha)^2$ curves appear. The spectrum of the film, at TT0 shows that the film has high transmittance (nearly 70%) in the

infrared region, but the value reduced after TT1 and TT2. The transmittance decreases down to ~20% and ~30% for TT1 and TT2, respectively, for the samples treated in N₂ atmosphere.

The transmittance is higher (~45% and ~55% for TT1 and TT2, respectively) for the samples treated in Ar atmosphere. In the visible part of the spectrum, transmission falls until, as expected, it reaches a dip in the ultraviolet region nearly at 350 nm [23]. It is worth noting that the transmittance of TT1 samples is always lower than TT2 samples, due to the residuals of the different intermediate phases observed prior to the complete formation of CZTS NCs. In fact, the XRD results of Figure 7 show the presence of SnS (PDF#39-0354) peaks in TT1 samples under N₂ atmosphere, and Cu₂S (PDF#65-2980) peaks in TT1 sample under Ar atmosphere.

In general, the reduction in transmittance of samples after TT1 and TT2 can be attributed to the growth of the CZTS NCs, with formation of native defects (e.g., vacancies, interstitial and anti-site). These defects generate absorption centres within the energy gap, which contribute to the photon absorption. In particular, the transmittance of the spurious phases in the films decreases strongly in the NIR region apparently due to a high density of shallow defects. It is also observed that the transmittance curve of the CZTS film shows a sloping trend, which could be caused by absorption of photons in deep centres generated by structural defects [24] [25]. The samples with thermal treatment under N₂ atmosphere showed higher reduction in transmittance as compared to samples with thermal treatment under Ar atmosphere. This might be due to SnS, formed under N₂ annealing, which has a low energy gap (1.14 eV) and could contain a large density of defects giving absorption in the IR range.

Moreover, also the difference of thermal capacity and conductivity between the two gases can account for the different microstructure of the films after the treatments. Ar and N₂ have similar diffusivity, but Ar is less conductive and capacitive than N₂. Thus, although both gases can be considered as inert in the treatment conditions, in N₂ atmosphere the heat is more efficiently transferred to the sample. However, as shown below, the different inert gas atmosphere seems to play no role in the treatments at lower (500°C) and higher (600°C) temperature.

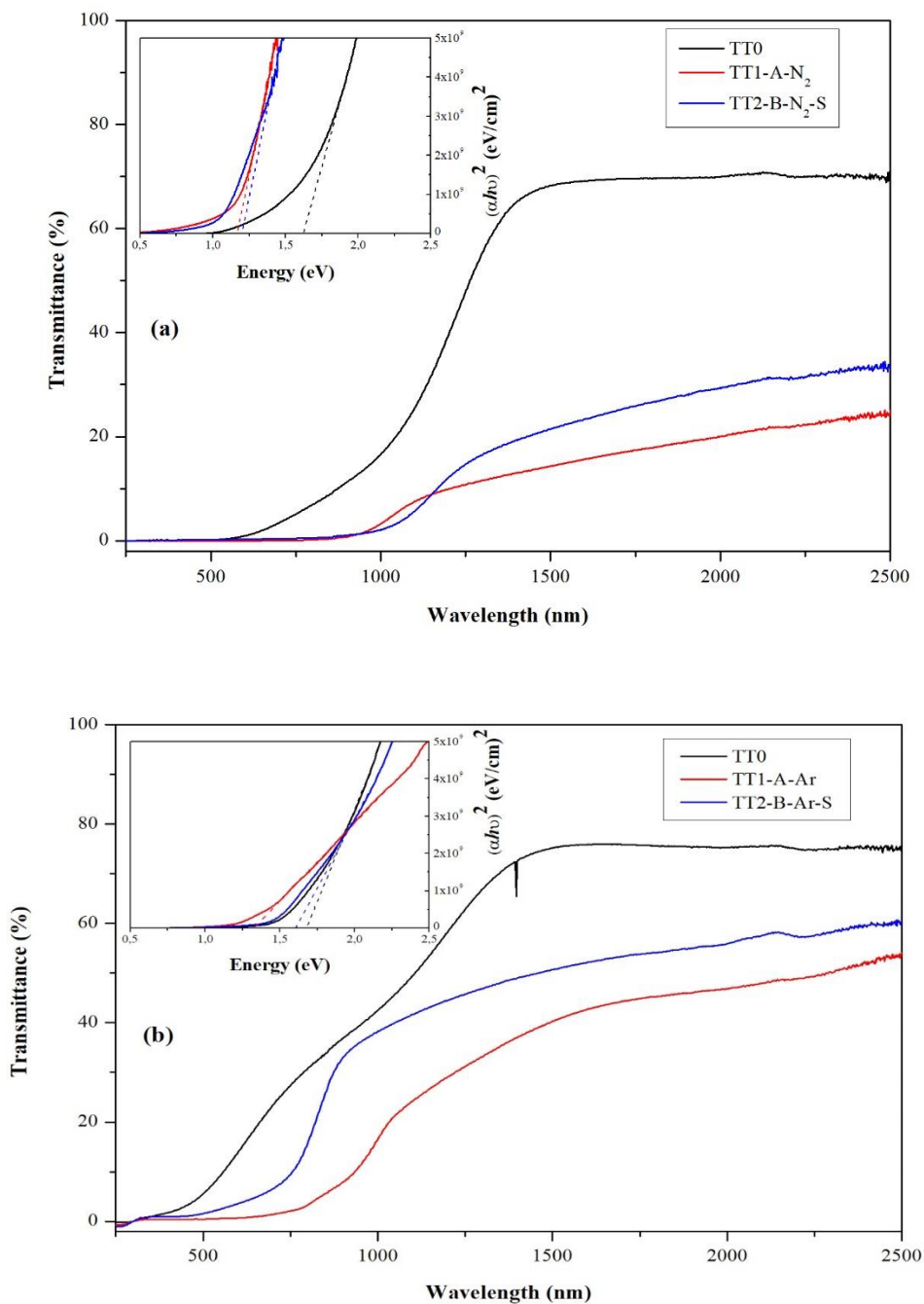


Figure 14 The UV-Vis transmittance spectrum of K2 sample at different thermal treatments (TT0, TT1 and TT2) and tauc plot for determination of band gap under: a) N₂ b) Ar atmosphere

Moving on to Tauc's plot, the bandgap energy values for samples treated under N₂ atmosphere are 1.6 eV, 1.16 eV, and 1.2 eV for TT0, TT1, and TT2, respectively. For samples treated under Ar atmosphere, the bandgap energy values are 1.6 eV, 1.3 eV, and 1.58 eV, for TT0, TT1, and TT2, respectively. The reduction of bandgap energy after TT1 and TT2 can be related to the reduction in transmittance caused by the grain growth. The value of bandgap energies after TT2 as observed in samples treated under N₂ is lower compared to sample treated under Ar. This is due to the presence of SnS and CTS as observed by Raman, which has a lower bandgap energy [26] than CZTS [27].

3.1.5.2 TT0→TT1-(C) →TT2-(D)

Figure 15 shows the XRD pattern of samples annealed at 500°C with a heating rate of 3°C/min (TT1), and a second thermal annealing at 600°C under sulphur vapour (TT2). High crystallinity was achieved after TT1 for both samples (TT1-C-N₂ and TT1-C-Ar). In addition, the secondary phase of SnS was detected. Differently from what observed at 560°C, this result seems almost independent of the gas used, Ar or N₂. The second thermal treatment in sulphur atmosphere results in the elimination of this spurious phases in both samples: films in final condition are made of pure tetragonal CZTS.

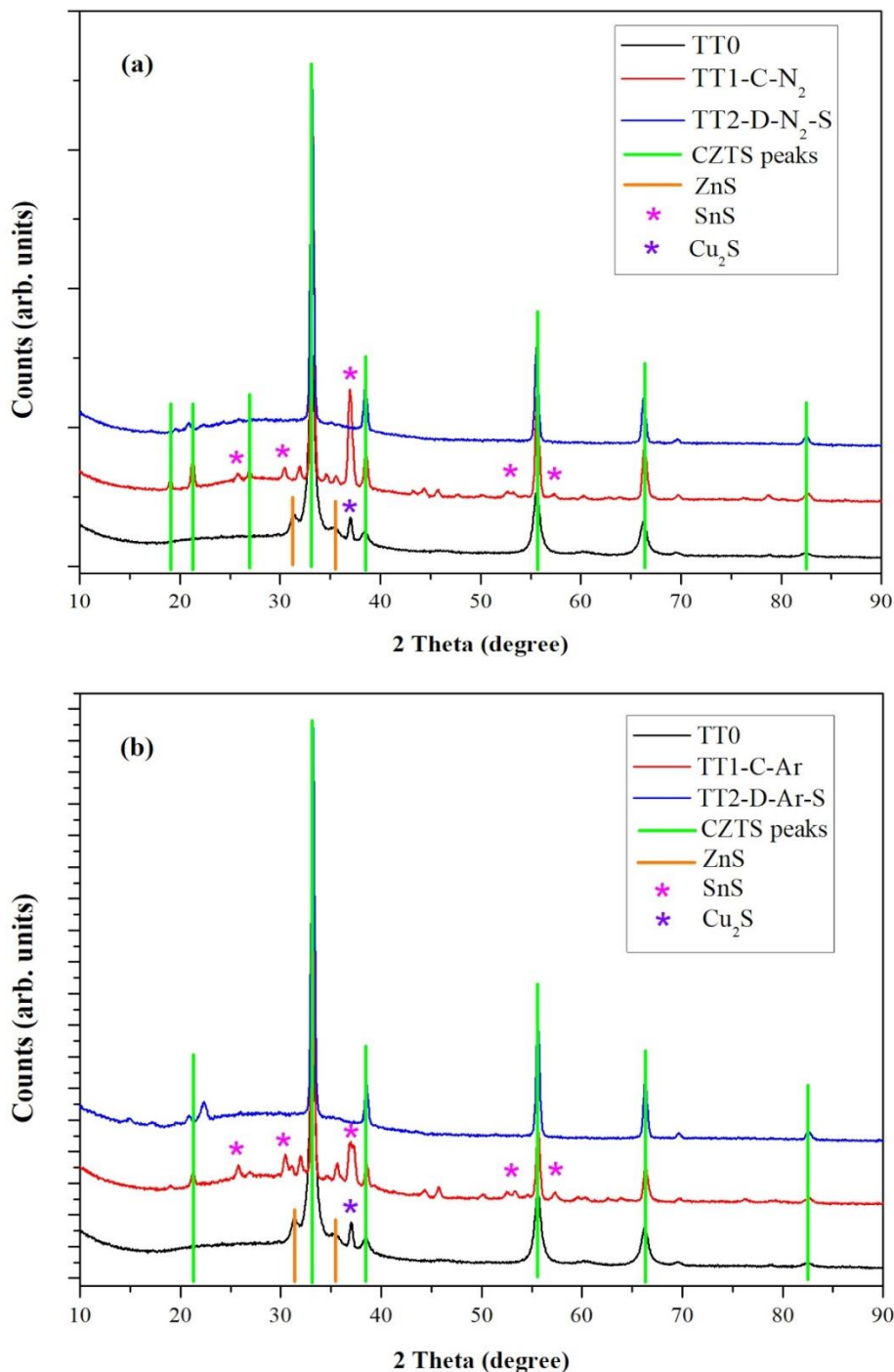


Figure 15 XRD pattern of samples annealed at 500°C with a heating rate of 3°C/min (TT1), and second thermal annealing at 600°C under Sulphur vapor (TT2) under: a) N₂ b) Ar atmosphere

The Raman spectrum of sample annealed at 500°C under argon atmosphere (TT1-C-Ar) is shown in Figure 16. A similar pattern can be observed as compared with Figure 9b, indicating the presence of both SnS and CTS secondary phases. However, the sample annealed under Ar atmosphere after TT2, shows $Cu_{2x}S$ phase at 500 cm^{-1} [28] which cannot be seen in XRD measurements. In addition, the peak of carbon ($1800\text{-}1000\text{ cm}^{-1}$) can be detected for both sample after TT2.

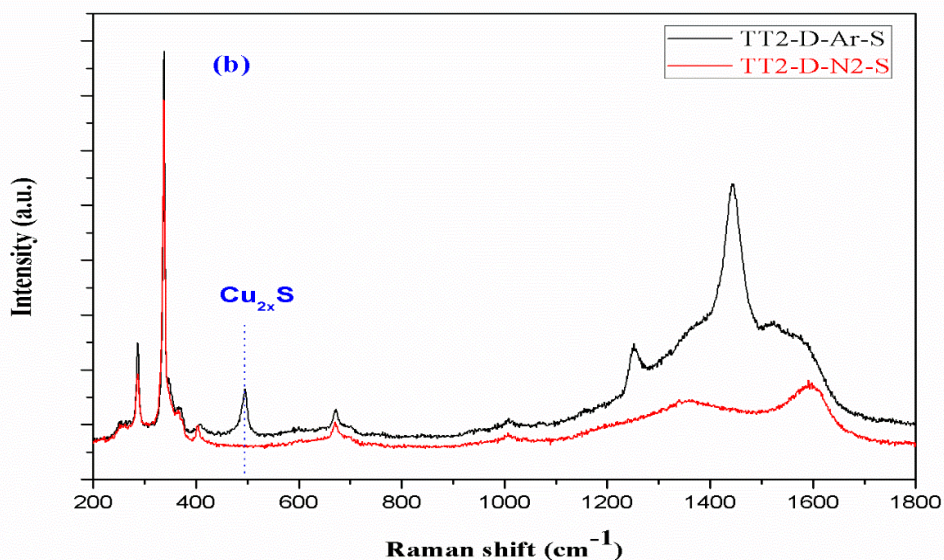
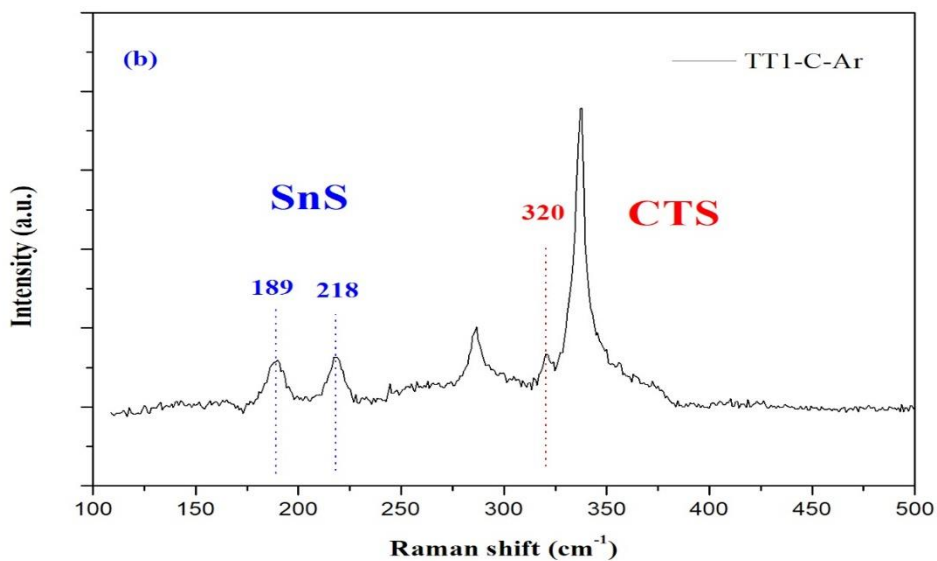


Figure 16 Raman spectra of sample a) TT1-C-Ar b) TT2-D-Ar-S and TT2-D-N₂-S

Figure 17 shows the SEM cross-sectional image of annealed samples (TT1-C) in N₂ and Ar atmosphere, respectively. Both SEM images revealed good grain growth and compactness of the CZTS layer. Annealing under Ar gas shows better homogeneity as compared with the sample annealed under N₂ atmosphere.

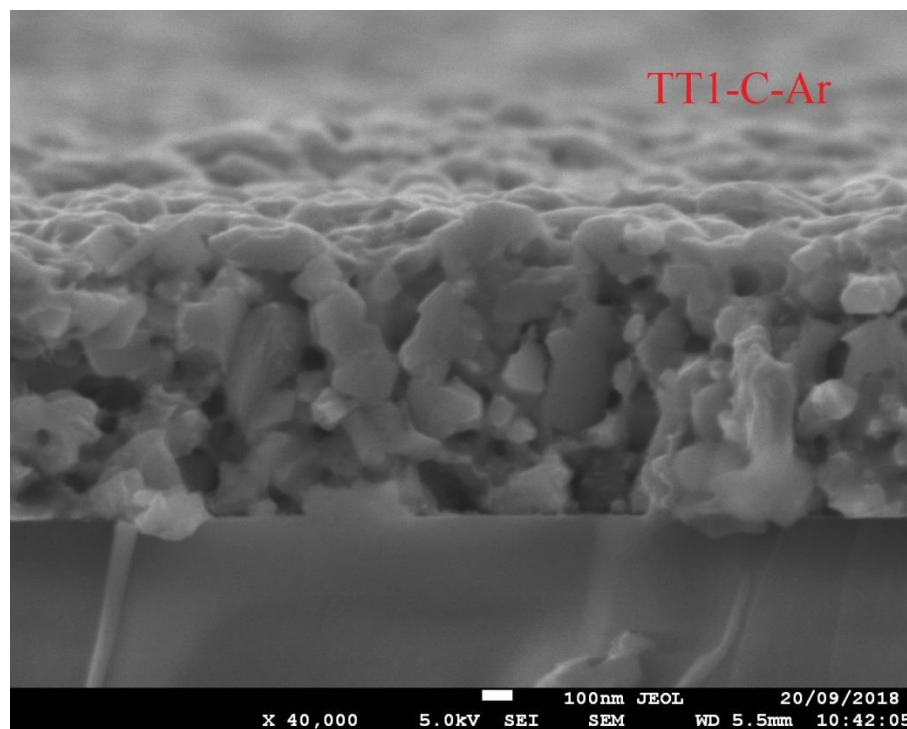
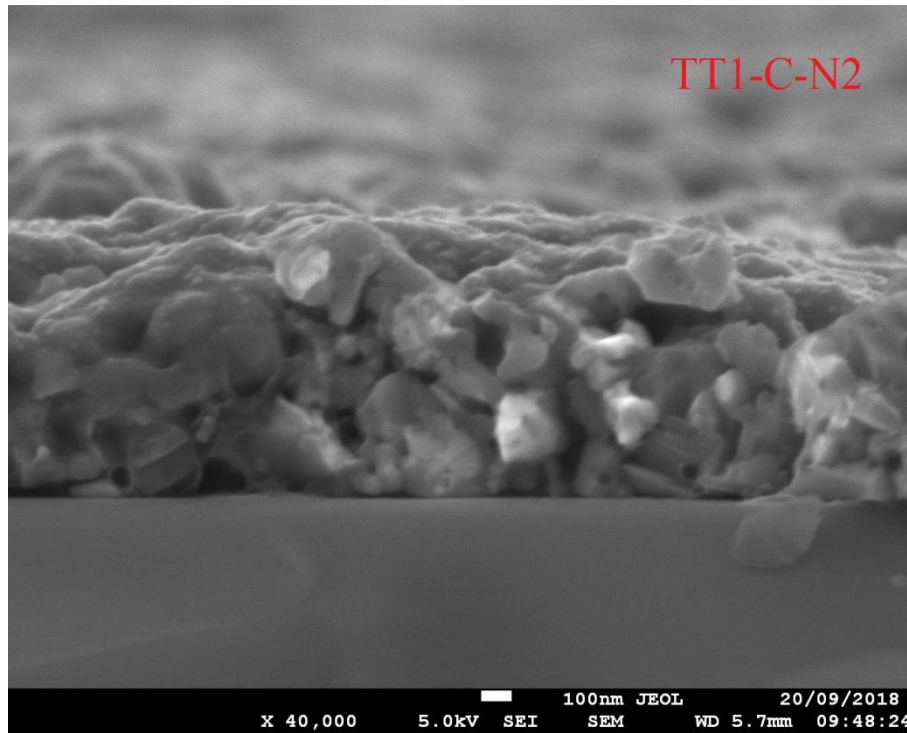


Figure 17 SEM image of annealed CZTS thin film after TT1 under different atmosphere: a) N₂ b) Ar

Figure 18 shows the transmittance spectra of as-deposited CZTS film (TT0), first thermal treatment (TT1) at 500°C, and second thermal treatment (TT2) at 600°C with S vapour. The figure shows transmittance curves of samples treated under: a) N₂ atmosphere and b) Ar atmosphere, each one together with the corresponding $(E\alpha)^2$ curve. The transmittance spectrum of films after TT0 shows a high transparency (nearly 70%) in the infrared region. However, as already observed before, the value reduced after TT1 and TT2. For samples treated in N₂ atmosphere, the transmittance is ~30% and ~40% in the infrared region, for TT1 and TT2 respectively. While samples treated in Ar atmosphere the transmittance is ~20% in the infrared region, for both TT1 and TT2. In the visible part of the spectrum, transmission falls slowly, until it reaches the expected dip in the ultraviolet region nearly at 350 nm.

As with the samples of Figure 14, the grain growth and the presence of secondary phases can account for the reduction of transmittance after TT1 and TT2, as well as for the increase in transmittance after TT2, when spurious phases disappear, although differences between TT1 and TT2 are not remarkable under Ar such as under N₂. This is probably due to the lower fraction of intermediate phases in the sample, as shown by the XRD of Figure 15.

For the Tauc's plot, the bandgap energy values for samples treated under N₂ atmosphere are 1.6 eV, 1.55 eV, and 1.58 eV for TT0, TT1, and TT2, respectively. For samples treated under Ar atmosphere, the bandgap energy values are 1.6 eV, 1.25 eV, and 1.23 eV, for TT0, TT1, and TT2, respectively. The reduction of bandgap energy after TT1 and TT2 samples for Ar atmosphere can be related to the reduction in transmittance due to Cu₂xS and carbon contamination.

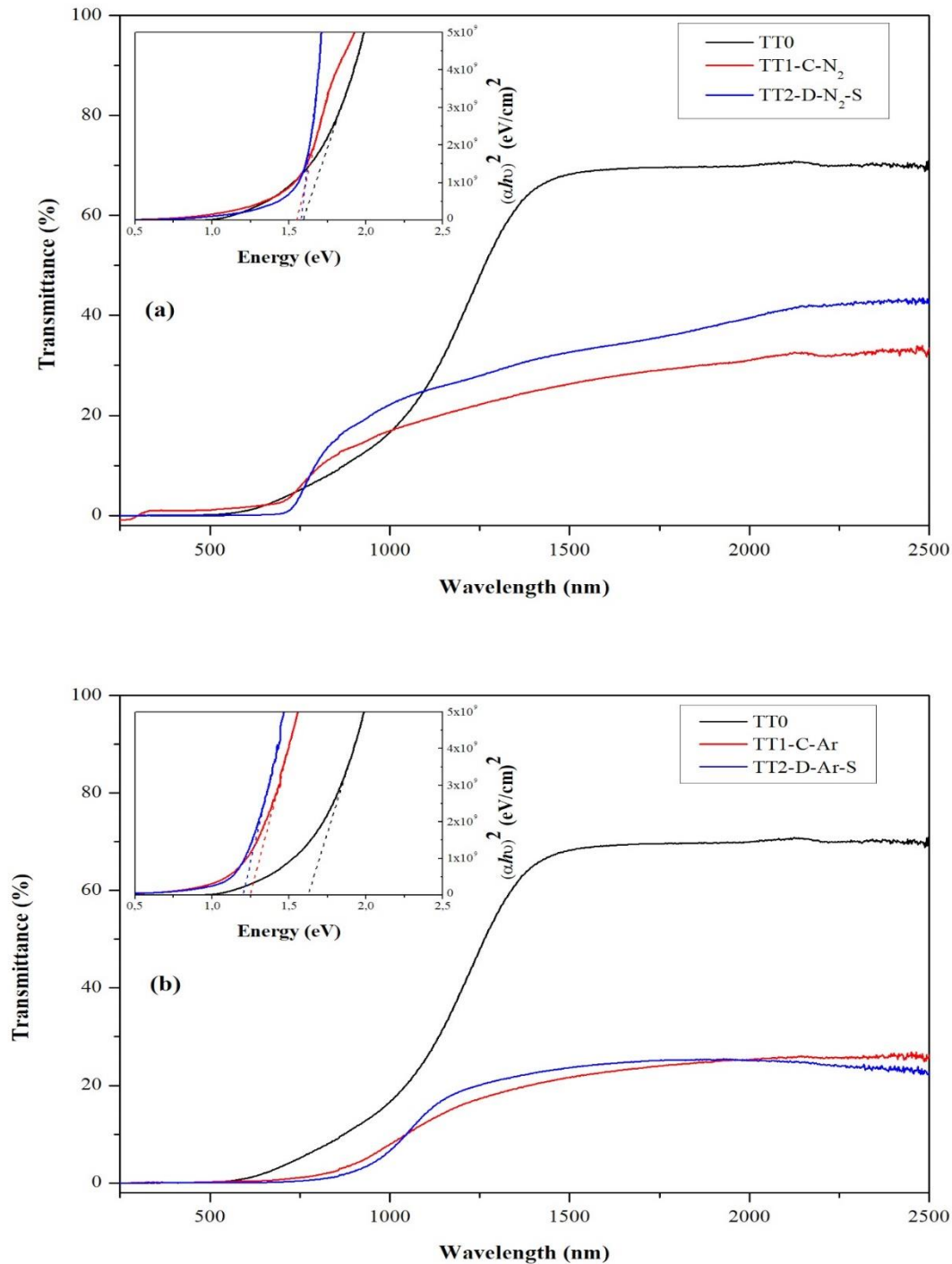


Figure 18 The UV-Vis transmittance spectrum of K2 sample at different thermal treatments (TT0, TT1 and TT2) and Tauc's plot for determination of band gap under: a) N₂ b) Ar atmosphere

3.1.5.3 TT0→TT1-(D) →TT2-(D)

Figure 19 shows the XRD pattern of samples annealed at 600°C with a heating rate of 3°C/min (TT1), and second thermal annealing at 600°C under sulphur vapour (TT2). Annealing at high temperature (600°C) in TT1 slightly improved the crystallinity and caused the appearance of Cu₂S (PDF#65-2980) as secondary phase. This result seems to be almost independent of the type of gas (Ar and N₂), since similar findings were observed on in the corresponding samples obtained with the different atmospheres. In both samples,

annealing with sulphur vapour (TT2) was able to eliminate the secondary phases, leading to formation of tetragonal CZTS only.

Putting together all results, our observations indicate that the annealing at 500°C leads to the formation of SnS (Figure 15) whereas at higher temperature (600°C) Cu₂S appears, independently of the type of inert gas (Ar or N₂) used. Treatments at 560°C are in a transition region where even minor differences lead to formation of SnS or Cu₂S. Whether this should be ascribed to different physical properties of the two gases (as heat capacity and conductivity are indeed different), or to the effect of contaminations (as all technical gases inevitably carry some different species), is still to be understood.

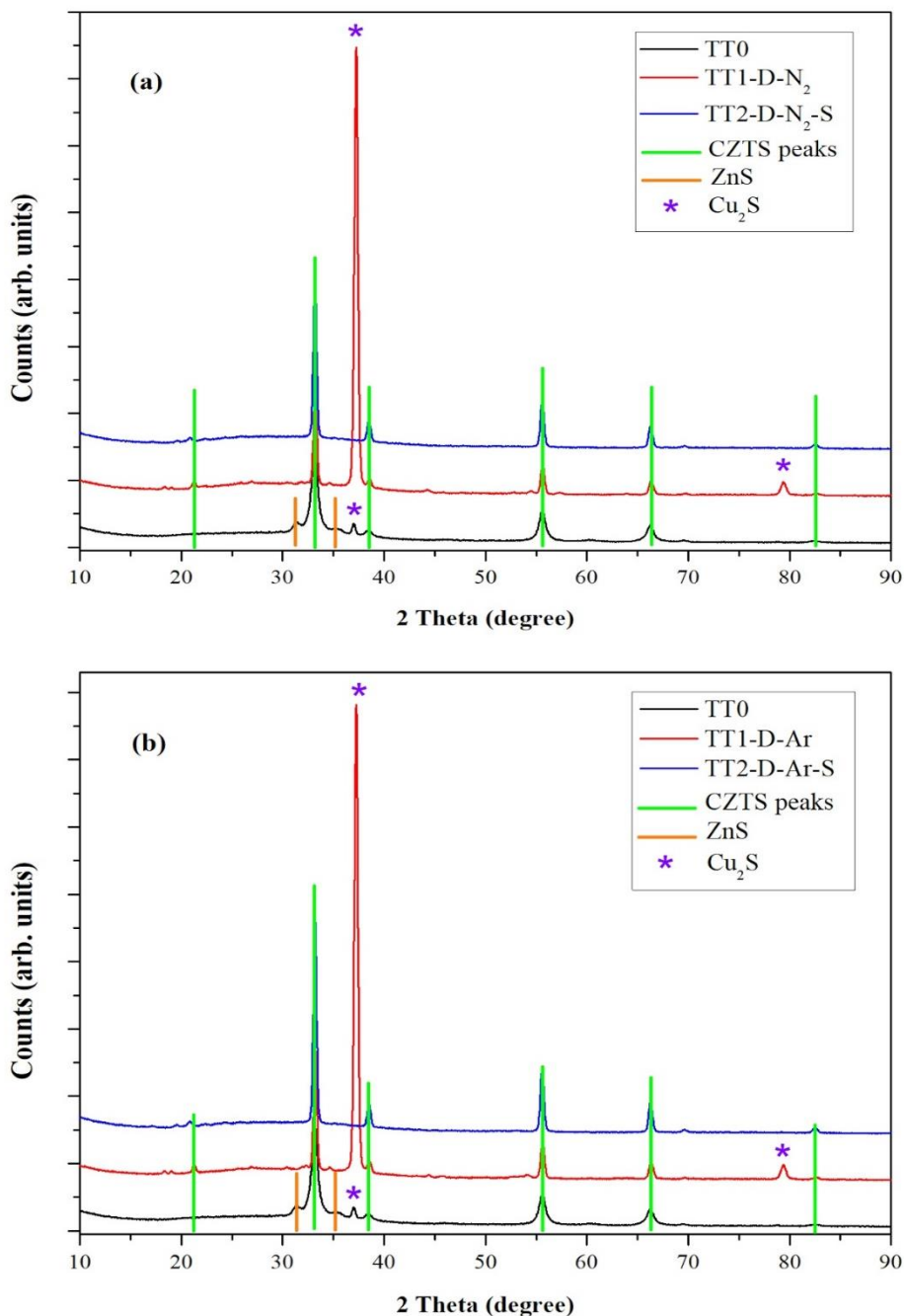


Figure 19 XRD pattern of samples annealed at 600°C with a heating rate of 3°C/min (TT1), and second thermal annealing at 600°C under Sulphur vapor (TT2) under: a) N₂ b) Ar atmosphere

Figure 20 shows the Raman spectrum of sample annealed at 600°C under argon atmosphere, with a visible peak at 337 cm^{-1} , typical of CZTS. Even if XRD revealed the formation of Cu_2S after thermal treatment at 600°C, no corresponding signal is detectable in the Raman spectrum after TT1 and TT2, as with many other $\text{Cu}_{(2-x)}\text{S}$ phases. Moreover, it is likely that the phase evidenced by XRD spectra differs from that reported in the literature. However, carbon peak (1800-1000 cm^{-1}) clearly can be seen on both samples after TT2. It is put forward, however, that XRD certainly refers to the whole thickness of the film, whereas Raman is more sensible to the surface phases; this feature further adds to the complementarity of the two techniques, which is quite useful in the context of the present work, and will be exploited also in the future.

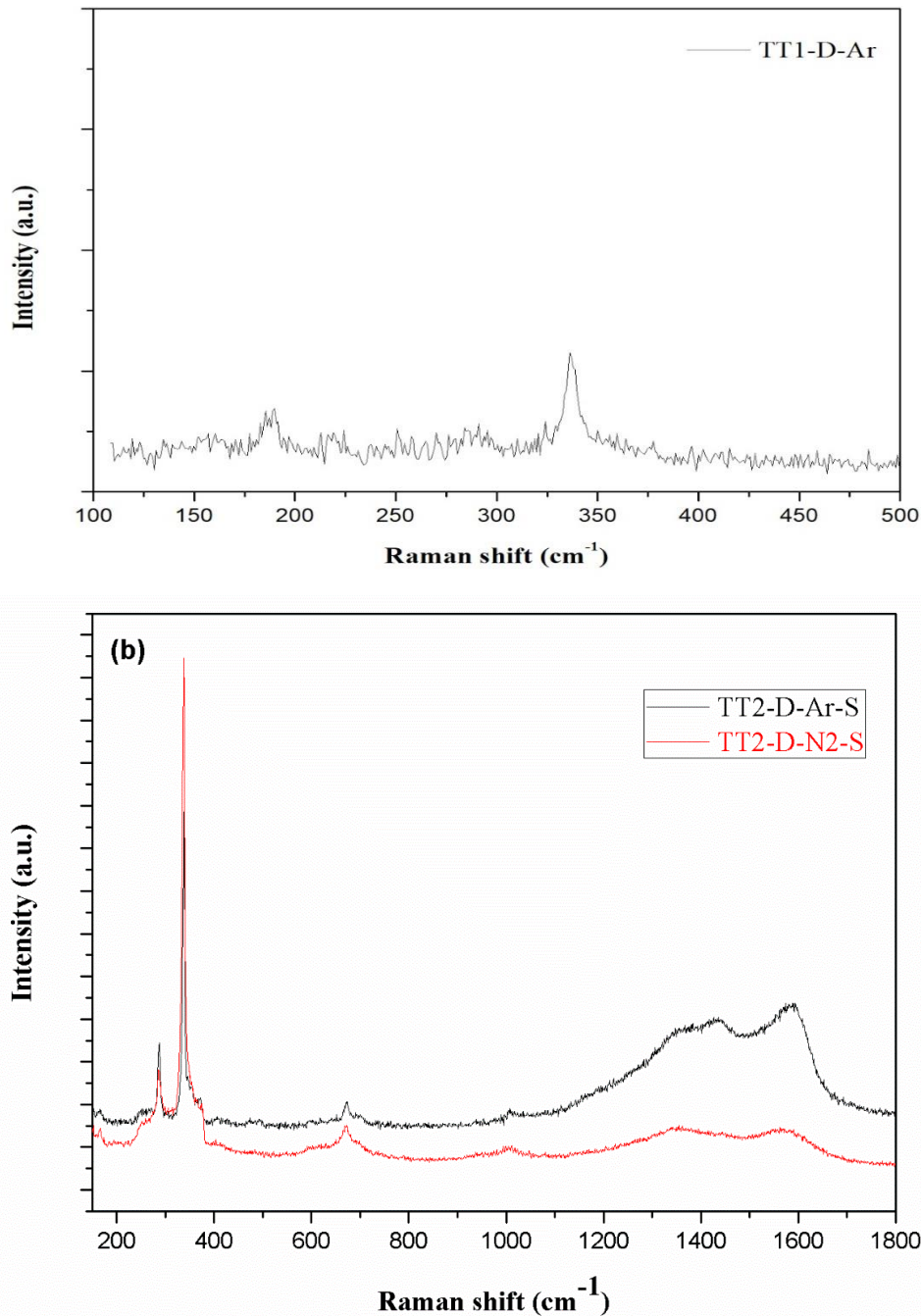


Figure 20 Raman spectrum of sample a) TT1-D-Ar b) TT2-D-Ar-S and TT2-D-N₂-S

The morphology of the samples annealed at 600°C with heating rate of 3°C/min under different inert atmosphere (N₂ or Ar) is shown in Figure 21. The cross-sectional images of the annealed samples show that grain growth occurs uniformly through the film, regardless of the type of annealing atmosphere.

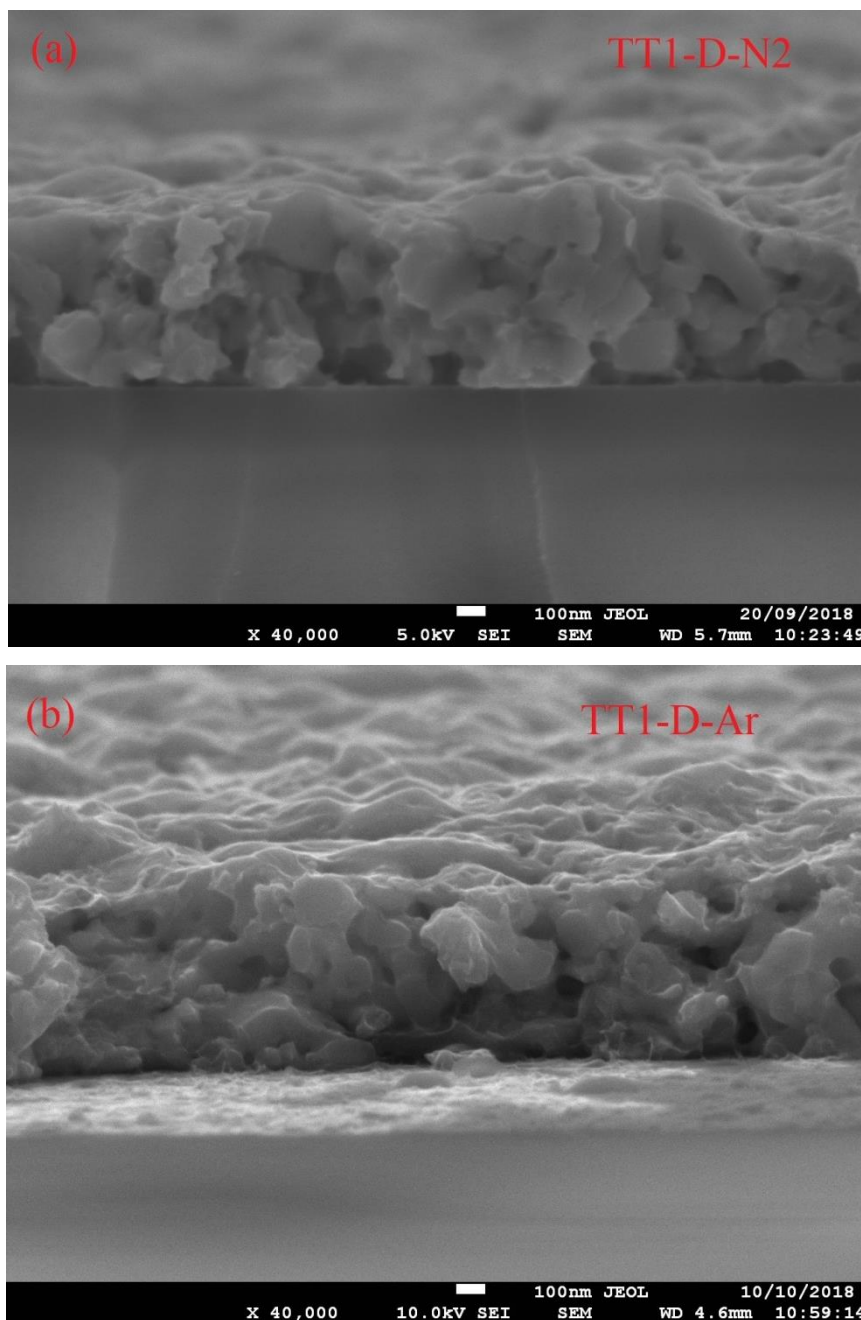


Figure 21 SEM image of annealed CZTS thin film after TT1 under different atmosphere: a) N₂ b) Ar

The transmittance spectra of as-deposited CZTS film (just after TT0), first thermal treatment (TT1) at 600°C, and second thermal treatment (TT2) at 600°C with S are shown in Figure 22 for N₂ (a) and Ar (b) atmosphere. The figure includes, for each sample, the corresponding $(E\alpha)^2$ curve.

The transmittance spectrum of films after TT0 shows a high transparency (nearly 70%) in the infrared region. However, the value reduced, as observed with treatments at lower temperatures, after TT1 and TT2. For samples treated in N₂ atmosphere, the transmittance is ~20% and ~30% in the infrared region, for TT1 and TT2, respectively; whereas the transmittance of samples treated in Ar atmosphere is ~18% and ~30% in the infrared region for TT1 and TT2, respectively.

In the visible part of the spectrum, transmission slightly falls until it reaches the expected dip in the ultraviolet region at about 350 nm. As observed in Figure 14, also in this case the grain growth and the

presence of secondary phases can account for the reduction of transmittance after TT1 and TT2, as well as the increase in transmittance after TT2. For Tauc's plot, the bandgap energy values for samples treated under N₂ atmosphere are 1.6 eV, 1.5 eV, and 1.25 eV for TT0, TT1, and TT2 respectively. For samples treated under Ar atmosphere, the bandgap energy values are 1.6 eV, 1.22 eV, and 1.21 eV, for TT0, TT1, and TT2 respectively. The reduction of the bandgap energy after TT1 can be due to the annealing at 600°C without Sulphur, which is able to induce a partial decomposition of CZTS, with SnS evaporation and formation of Cu₂S; this picture is coherent with the observed bandgap values, as the bandgap of Cu₂S [29] is lower than that of kesterite CZTS [27]. The following TT2 treatment mainly restores the correct CZTS structure, but probably leading to a copper-rich composition, which is known to give samples with excess conductivity and low transmittance. It is also possible that the Cu₂S secondary phase becomes so much dispersed and ill-defined to be undetectable by Raman and XRD.

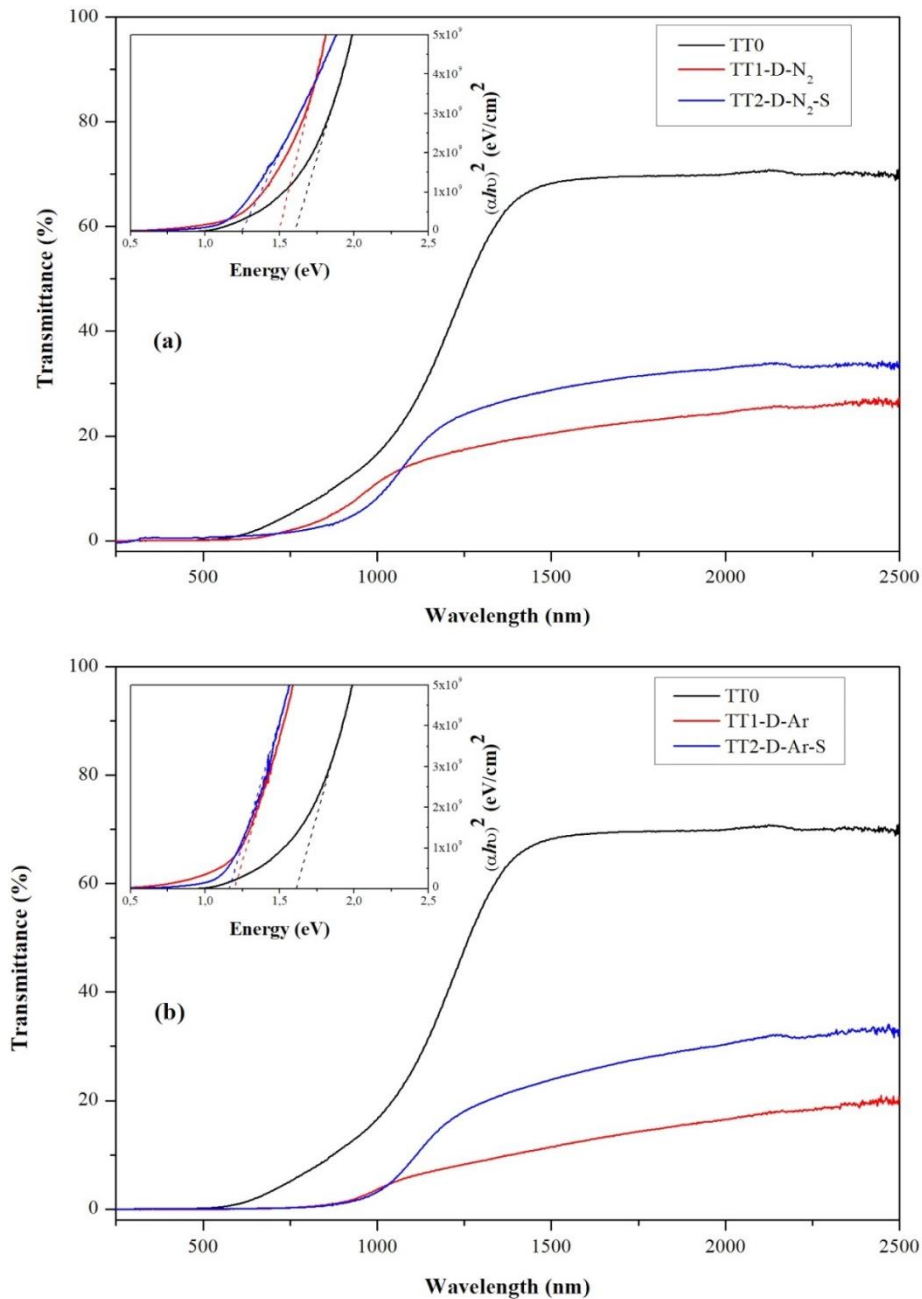


Figure 22 The UV-Vis transmittance spectrum of K2 sample at different thermal treatments (TT0, TT1 and TT2) and Tauc plot for determination of band gap under: a) N₂ b) Ar atmosphere

3.1.5.4 TT0→TT1-(C)S

The diffraction patterns displayed in Figure 23 correspond to sample annealed at 500°C with heating rate of 3°C/min, under Ar and N₂ atmosphere, respectively. A small amount of sulphur was added to the TT1 step to study the effect of sulphur on crystallization. Our previous observations indicate that grain growth is hindered by annealing in Sulphur atmosphere. In fact, Sulphur can cross-link OLA's carbon-carbon double bonds, preventing its pyrolysis and leaving organic residuals protruding from surface. These residuals act as spacers among the grains and prevent their growth. Two peaks at 2θ=15° and 22° were detected under N₂ atmosphere, which could be due to Cu₂S.

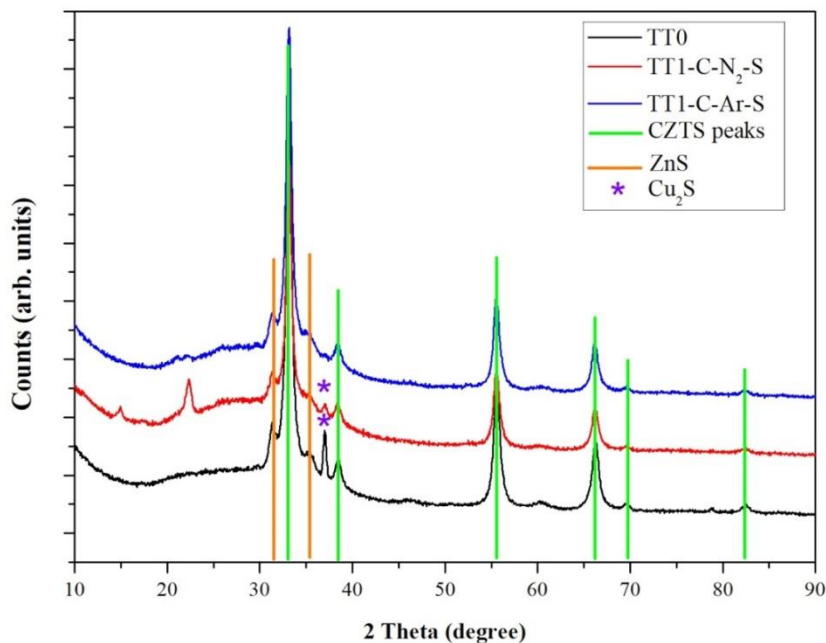


Figure 23 XRD pattern of samples annealed at 500°C with a heating rate of 3 °C/min (TT1) under Sulphur vapor

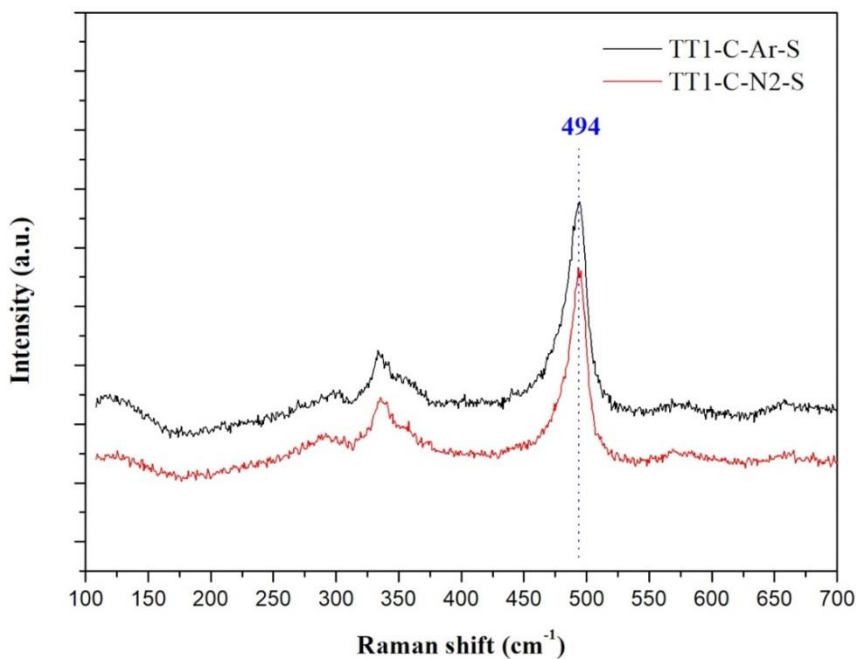


Figure 24 Raman spectra of samples: TT1-C-Ar-S and TT1-C-N2-S

Figure 24 shows the Raman spectra of the CZTS films annealed at 500°C under the two different atmospheres. Both patterns show a sharp peak at 494 cm^{-1} , which is attributed to the Cu_2S phase [30]. This result is in good agreement with XRD data and shed more light on the presence of secondary phases.

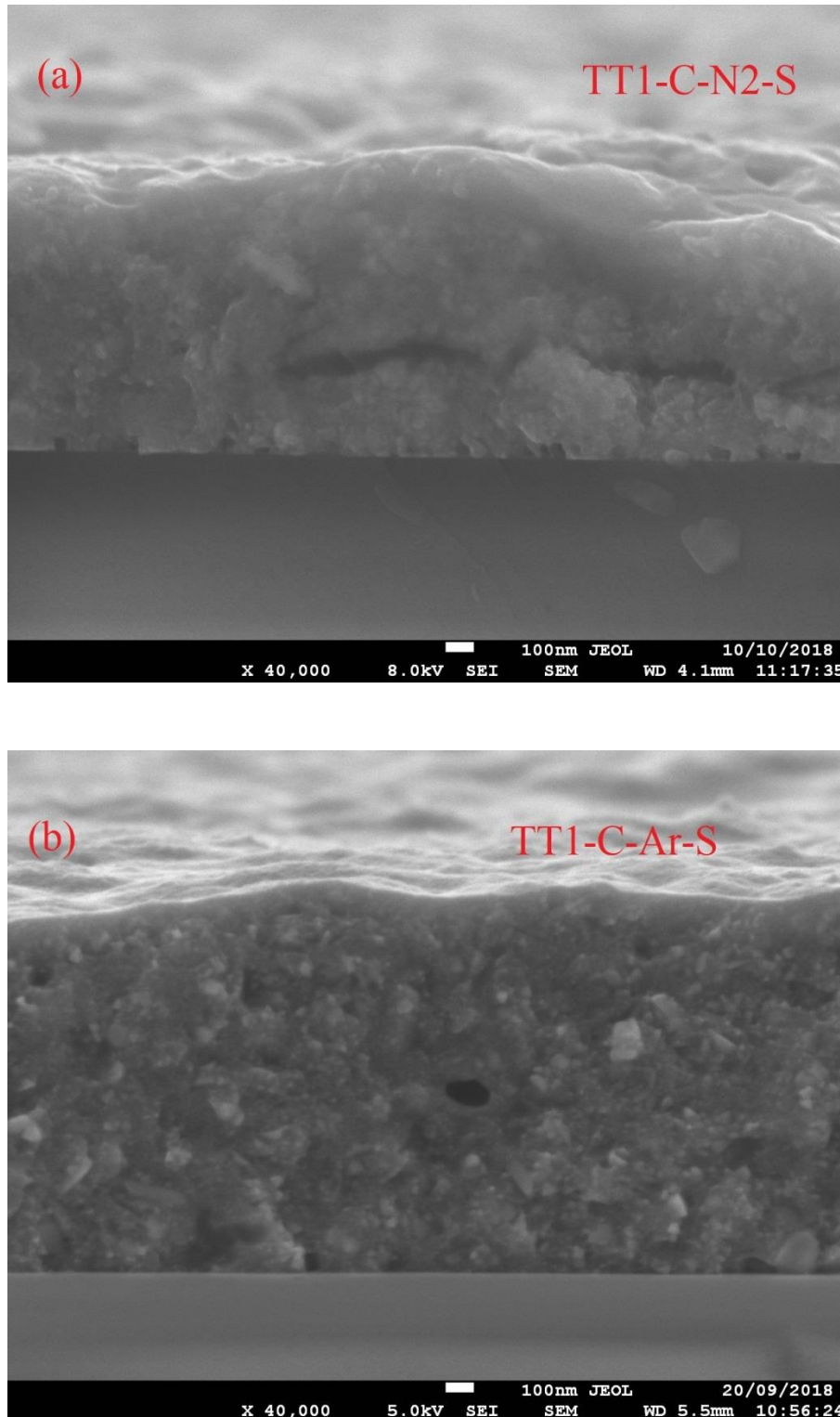


Figure 25 SEM image of annealed CZTS thin film after TT1 under different atmosphere: a) N2-S b) Ar-S

SEM cross-sections of CZTS films thermally treated with sulphur under N₂ and Ar atmosphere are shown in Figure 25 a and b, respectively. As it can be seen, the grains did not grow, in accordance with the XRD measurements showing broad peaks. In fact, after deposition the nanocrystals are still surrounded by the organic solvent used for the ink production. Upon annealing at high temperature, the solvent should evaporate, and then be removed through interaction with sulphur vapour forming COS or CS₂ and H₂S [31]. However, with OLA a fraction of solvent which is not removed by the thermal treatments forms a coating layer blocking the growth of the CZTS nanocrystals.

3.1.6 Carbon analysis

The quantitative elemental analysis was performed on the K2 samples using the CHN analyser by LECO, both after soft thermal treatment (TT0) and after high temperature treatment (TT2). Results point out a high content of carbon in the soft annealed samples, about 20%, which drops to almost 9% after the high thermal treatment. GDOES measurements were also carried out to measure the carbon content after the different thermal treatments: the typical elemental depth profiles measured in CZTS films after TT0 and TT2 are shown in Figure 27

Carbon after the soft annealing (TT0) gives a high signal (Figure 27a), but it is worth considering that the measurement refers to a rather thin sample (100 nm), so it is biased by the high amount of carbon localized on the surface. The measurement after TT2, instead, was performed on a 'standard' (~1.5 μm) sample and shows a marked drop in the carbon signal (Figure 27b) expected after the high temperature treatments. As with previous preparations, these results show that the organic residues, still present in the starting materials after the drying treatment at 150°C, can be reduced upon annealing at high temperature. Although the absolute carbon concentration cannot be quantified using the GDOES signal, it is possible to compare the carbon amount in different samples using the C/S ratio. The results indicate a C/S ratio between 6 and 10 after TT0, falling down to 0.6 – 0.8 after TT2. The latter values are not far from those of previous preparations.

However, contrary to what observed in samples made using OLA solvent only, SEM shows that in this case carbon contamination does not significantly affect the grain growth. The fraction of carbon which remains after high thermal treatment suggests that the organic residuals cannot be fully eliminated by pyrolysis but, as a matter of fact, do not prevent the formation of a uniform, well-adhered, crack-free layer made of well-crystallized CTZS grains, which is the main goal of this work.

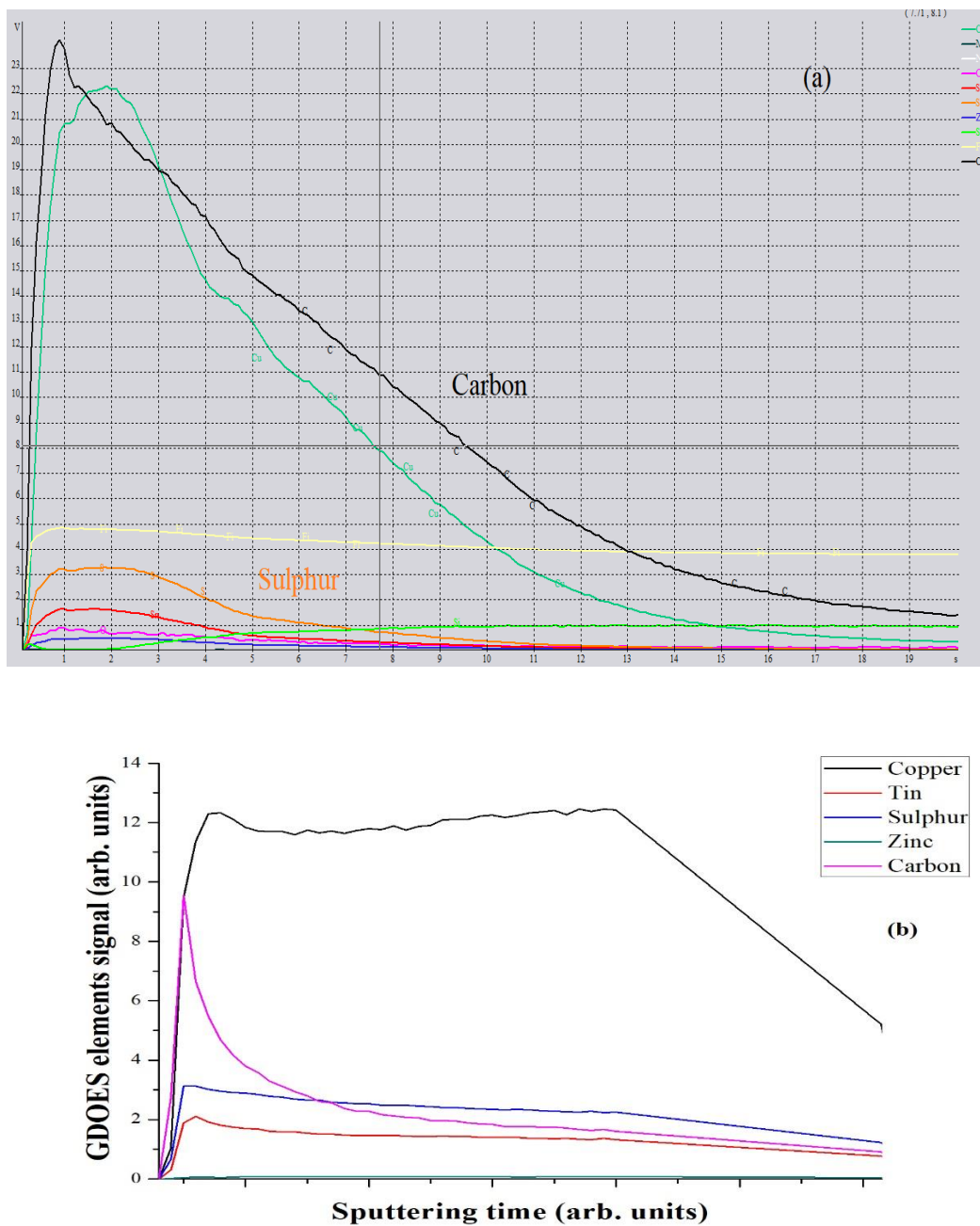


Figure 26 GDOES depth profiles (raw data) of CZTS elements measured after a) the soft treatment (TT0) on a thin film (100 nm), and b) after the high temperature thermal treatment (TT2) of a regular (ca 1.5 μm) layer

3.1.7 Resistivity

Resistivity measurement were made on several samples after different thermal treatment, using a 4-point probe. In addition to the resistivity values, Table 3 contains the description of the thermal treatments and the values of the band gap energy (E_g) and of the transmittance at 1500 nm after TT1 and TT2. The type of spurious phases detected by XRD after TT1 and by Raman after TT2 are also reported.

Samples S1(Ar) and S2(N₂) are better than the others in the sense that Raman measurements cannot detect spurious phases after TT2; the correct (expected) gap value and greater resistivity point to the formation of CZTS phase without a large defect concentration. Samples S1(N₂) and S2(Ar) show a low gap and a low resistivity due to the presence of spurious phases. Samples S3(N₂) and S3(Ar) also show a low gap and a low resistivity but secondary phases were not detected, neither by XRD nor by Raman, after TT2. As discussed above a possible explanation is that TT1 annealing at 600 C without Sulphur can induce a partial decomposition of CZTS with SnS evaporation and formation of Cu₂S. As already pointed out above, the following TT2 treatment mainly restores the correct CZTS structure but possibly with a copper rich composition which is known to give samples with excess conductivity and low transmittance. It is also possible that the Cu₂S secondary phase becomes so much dispersed and ill-defined to be undetectable by Raman and XRD. In any case it is clear that the TT1 annealing temperature must be maintained below 560 C.

Table 3 Resistivity of samples after different thermal treatments. The values of the band gap energy (E_g) and of the transmittance at 1500 nm after TT1 and TT2, the type of spurious phases detected by XRD after TT1 and by Raman after TT2 are also reported.

sample	TT1 Temp (°C)	TT1 spurious phase	E _g (TT1) (eV)	T(TT1) (at 1500 nm)	TT2 temp (°C)	TT2 spurious phase	E _g (TT2) (eV)	T(TT2) (at 1500 nm)	Resistivity (ohm cm)
A-B (N ₂)	560	SnS	1.16	15%	560	SnS,CTS	1.2	20%	0.012
A-B (Ar)	560	Cu ₂ S	1.3	50%	560	-	1.58	40%	2.6
C-D (N ₂)	500	SnS	1.55	25%	600	-	1.58	30%	1.05
C-D (Ar)	500	SnS	1.25	25%	600	Cu ₂ S	1.23	25%	0.004
D-D (N ₂)	600	Cu ₂ S	1.5	20%	600	-	1.25	30%	0.016
D-D (Ar)	600	Cu ₂ S	1.22	10%	600	-	1.21	25%	0.023

4

Kesterite powders made by high-energy ball milling as precursors of solar inks.

In this section of the report we show that it is possible to produce kesterite (Cu₂ZnSnS₄) powders by an alternative process, with a cost even lower than “hot-injection”: high-energy ball milling. Starting from a stoichiometric mixture of Cu, Zn, Sn, S, by reactive grinding at high energy in a planetary mill CZTS form progressively but takes a cubic structure instead of the equilibrium tetragonal structure. Grinding beyond 60 minutes, using the currently adopting milling parameters, leads to an increasing contamination from the milling vials, in the form of small particles of brass.

This study, although still preliminary, paves the road to the production of solar inks for absorber layers in thin film solar cells, based on a low-cost alternative to the hot-injection synthesis investigated so far.

4.1 Experimental

The CZTS powders were made by reactive high-energy grinding in a planetary mill (Fritsch P4 Pulverisette 4), using 80 ml jars of brass and 25 ball of the same material, with diameter of 12 mm.

Precursors, stoichiometrically weighted, are: Cu powder, <math><75\mu\text{m}</math>, 99%; Zn powder, purum, 99%; Sn powder, puriss, 99%, S flakes, purum, 99.5%; all provided by SigmaAldrich. The ball/powder ratio was kept fixed to 100:1 in weight, adding 250 μl of ethanol (99.8%, SigmaAldrich) as lubricant. These conditions, as well as those concerning mill rotations, were taken from analogous studies made by our Operating Unit (OU) of several ceramic materials, like gypsum, calcite and fluorite [32]. According to those studies, the jar rotation was fixed to $\omega = -540$ rpm, while the revolution of the main disk was $\Omega = 300$ rpm, so to give a ratio $\omega/\Omega = -1.8$. Grinding cycles consisted of single batches, with increasing duration of 15, 30, 60, 90 and 180 minutes, respectively.

The powders were analyzed by X-ray Diffraction (XRD) using a Rigaku PMG diffractometer, equipped with bent single-crystal graphite monochromator in the diffracted beam, using Cu $K\alpha$ radiation produced at 40 kV and 30 mA. The powder pattern was collected in the range $8 - 82^\circ$ (2θ), with a counting time of 10 s for each sampling step of 0.05° .

4.2 Results and discussion

The XRD patterns of the powders made by milling with increasing time are shown in Figure 27, with the indication of the phases identified by a Search-Match procedure based on the ICDD database. As an example of pattern modelling. Figure 28 shows the result for the powder ball milled for 60'. The modelling was made with TOPAS, using a beta version 7, which supports the new Macros developed by our OU, based on the Whole Powder Pattern Modelling (WPPM) [33]. This feature provides the size of the crystalline domains assuming an equiaxial (spherical) shape with a lognormal distribution of diameters [34].

As it is known, kesterite, ($\text{Cu}_2\text{ZnSnS}_4$, CZTS) has a tetragonal equilibrium structure with Space Group (SG) $I\bar{4}$, but in recent times, also according to our own research work, a hexagonal form was also obtained with SG P63mc. So far, the hexagonal polymorph was supposed to be stabilized by the very fine dimensions of the nanocrystals, which tend to assume a prismatic shape with hexagonal basis. This was verified in the hot-injection synthesis, which is a bottom-up process [35]: apparently ball milling takes to different results.

As shown qualitatively in Figure 27, the CZTS phase is already formed after 15'milling, although the synthesis is still largely incomplete at this stage: the corresponding XRD pattern shows the peaks of the precursors (Sn, S, Zn and Cu) together with those from an intermediate copper sulfide, covellite, CuS. In this stage CZTS seems to take a cubic structure, like that of sphalerite (ZnS), a structure which can be observed increasingly better with the increasing time of the milling process. The diffraction peaks of CZTS appear broad and diffuse, corresponding to a domain size of the order of 1 – 2 nm.

It cannot be excluded the presence of ZnS, as it would give diffraction peaks completely overlapping the main ones of kesterite; however, based on stoichiometry and on simple mass balance, it can be put forward that the main fraction of sphaleritic phase is a Sn-poor CZTS. Tin, in fact, appears for more than 80% in the form of metallic precursor, probably as a consequence that the starting powder was made of large particles, much slower in the reaction with Sulphur than the other two metals.

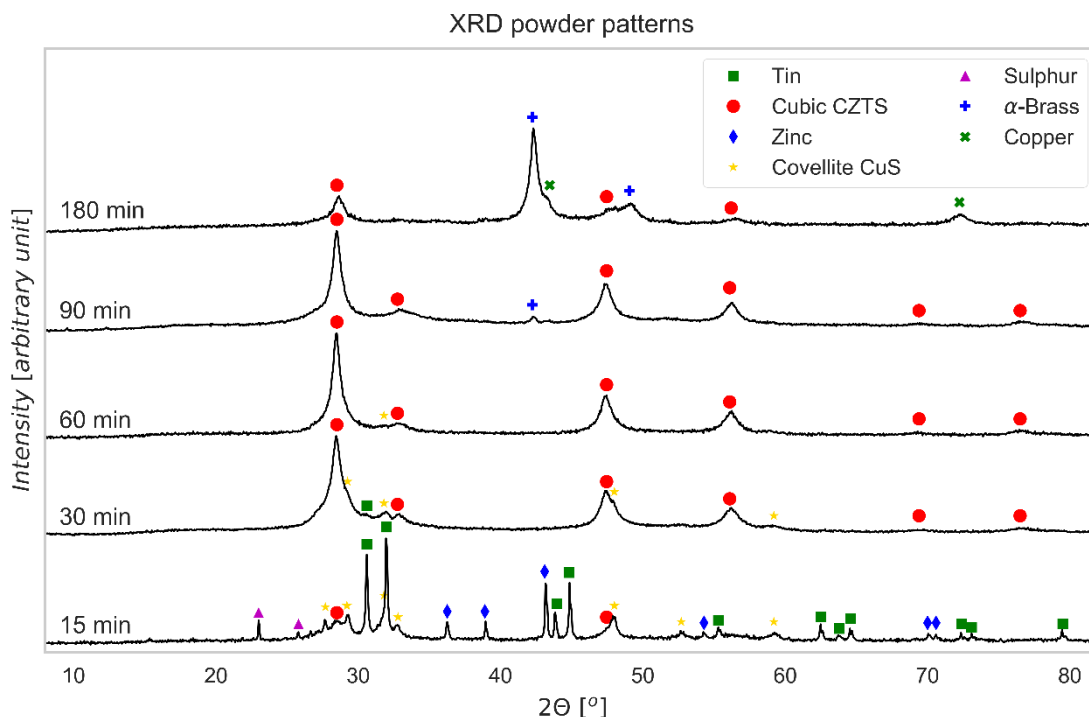


Figure 27 XRD patterns of the powders ground by high-energy milling in a planetary mill for increasing time. Symbols indicate peaks which identify the different crystalline phases

The presence of precursors and simple (i.e., binary) sulphides tends to disappear with longer grinding. Starting from 30' the CZTS fraction is the main one, even though a relatively small amount of metallic, unreacted Sn is still present together with some CuS. After 60' milling the CZTS phase approaches 100%, with a minor residual of CuS, quantified in about 1.5%. Longer grinding times lead to a complete disappearance of phases other than CZTS, but with the currently used brass vials a progressive contamination is observed. A metallic phase identified as brass appears, from the wear of jar and balls.

It is interesting to underline that kesterite produced by this reactive grinding procedure is not tetragonal, but seems to take a cubic form, like sphalerite (S.G. $F\bar{4}3m$). To verify this occurrence, we also made some annealing tests of the powder (in loose form or as tablet) which unequivocally show the formation of the equilibrium tetragonal CZTS form (S.G. $I\bar{4}$). We can put forward that the highly disordered condition of cations in the reactive milling process is responsible – in addition to possible deviations of the stoichiometry – for the stabilization of a cubic CZTS. Indeed, the relation between the two phases is quite simple: the transition toward the stable tetragonal phase happens on thermal treatment, by a doubling of the c axis of the cubic cell (tetragonal CZTS can thought of as made of two cubic cells one on top of the other), according to the relation $c = 2a$.

Based on a literature search cubic CZTS has never been produced at low temperature. Some authors report of cubic CZTS, but only at high temperature, in excess of 800°C [36] [37] [38], and made by quite different and more complex methods, like solution phase reaction [6] solid state reaction [39], vapor deposition [40] [41]. All those techniques involve high temperature, whereas our reactive milling is made at a nominally room temperature.

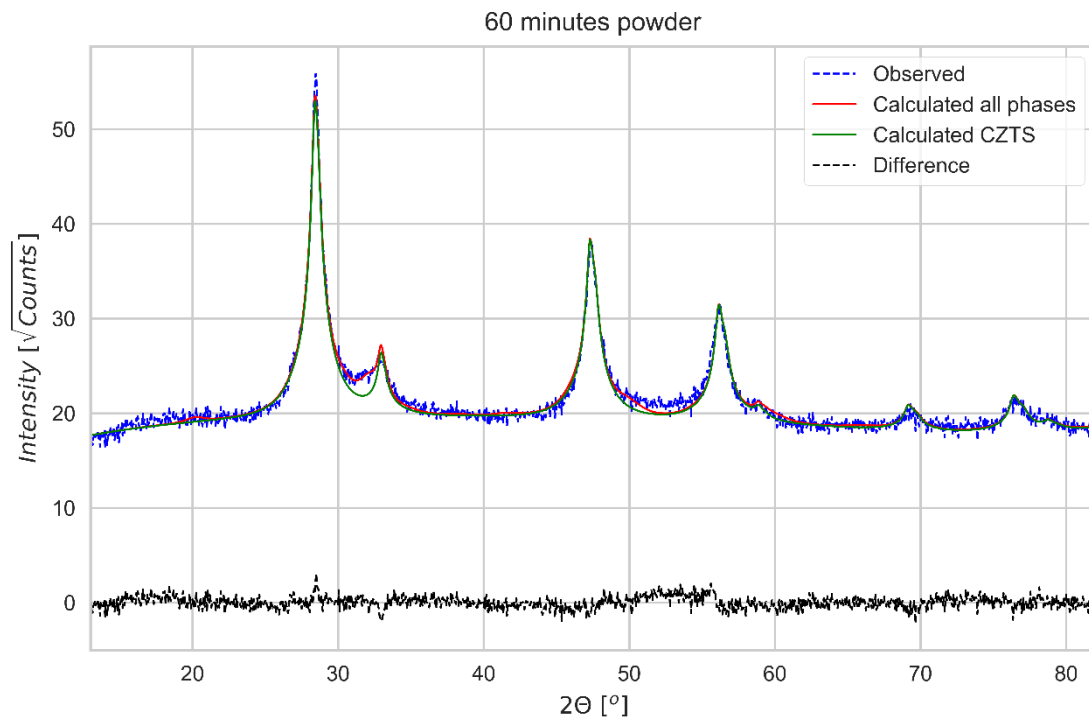


Figure 28 XRD pattern of the powder ground for 60', analyzed by Topas, version 7©, considering the phases identified in Figure 27. The CZTS phase is indicated in green, whereas the residual, difference between experimental data (blue) and total model (in red), is shown below (in black)

5 Conclusions

In the first section of the report we discuss the formation of a pure sulphide CZTS absorber layer with large grains starting from $\text{Cu}_2\text{ZnSnS}_4$ nanocrystals synthesised using a low-cost solution method based on metal chlorides.

CZTS NCs were previously obtained by a hot-injection process with elemental Sulphur, using oleylamine (OLA) as solvent. To improve the properties of the final CZTS films we tried to reduce the amount of carbon residuals replacing (at least partially) OLA with other solvents that can be easily removable during annealing at high temperature.

Two strategies were implemented: 1) use of DEG and TETA, and 2) use of OLA and 1-DDT.

The latter showed to be more effective since it was found that a certain amount of OLA is needed to control the morphology and adhesion of CZTS film.

Cracks in the film were an important issue to deal with, as they affected all previous preparations. Based on our present work, a suitable pre-annealing temperature, fine-tuned to relatively low temperature (150°C for 15 min), results in cracks-free thin films. Conclusive evidence is provided by microscopy.

XRD results revealed the presence of two phases (tetragonal CZTS and ZnS-wurtzite type) in the CZTS thin films after this pre-annealing. Dodecanethiol used in the reaction is supposed to be the key factor for the formation of the hexagonal (wurtzite type) phase. Dodecanethiol could react with the metal cations to produce metal thiolates, which would decompose into corresponding sulphides at certain temperature. These thiolates help to balance the different reactivity of cations in solution. Due to the strong coordination

with the metal cations exposing on the surface of nanocrystal, dodecanethiol also assists to passivate the obtained wurtzite CZTS. Dodecanethiol is supposed to adjust the chemical environment preferring the formation of the hexagonal structure. Secondary phase of Cu_2S formed in the early stage and then gradually transformed into wurtzite CZTS.

We also performed a comparative study to optimize the two crystallization annealing processes (the first TT1 without Sulphur and the second TT2 with Sulphur vapor) trying different temperatures (500°C, 560°C and 600°C), heating rates and type of inert gas (Ar or N_2) used in the treatment.

The present results indicate that performing the TT1 annealing at 500°C (3°C/min) leads to formation of SnS phase, whereas annealing at 600°C (3°C/min) causes the appearance of Cu_2S phase, independently of the type of inert gas (Ar or N_2) used in the treatment. Thermal treatments at intermediate temperature of 560°C (with heating rate of 20°C/min) leads to SnS secondary phase under N_2 gas, and Cu_2S under Ar atmosphere. At this temperature minor differences in gas properties and purity might shift conditions in favor of formation of one of the two simple sulfide phases, whereas at higher and lower temperatures stability of one of the two is more clearly demonstrated.

The second thermal treatment in the presence of Sulphur vapor, was an effective procedure to eliminate impurities (secondary phases), leading to well-adhering and crack-free films, favoring at the same time the grain growth. Crystal structure, morphology and optical properties of CZTS material were studied before and after annealing process, confirming the formation of the kesterite phase in the final films. We could also observe that N_2 gas in thermal treatments has slightly better effect on grain growth with respect to Ar gas.

The elemental analysis and GDOES measurements confirmed the reduction of carbon residual after high temperature thermal treatment. Overall the amount of carbon is still high after thermal treatments, but with the current procedure, based on using the mixed OLA+DDT solvent, grain growth seems little affected. It is put forward that carbonaceous residuals left by this procedure do not form a coating of CZTS nanocrystals, at least not to the point of blocking the growth as observed in our previous work based on OLA solvent only.

UV-vis spectroscopy studies were performed to investigate absorption and band gap of CZTS films after different thermal treatments. The band gap energy of as-synthesized CZTS is consistent with the literature values of 1.5 eV. This value is sometimes reduced (~1.2 eV) after post-annealing due to appearance of spurious phases or defects in the CZTS film. However, thermal treatment under N_2 gas with heating rate of 3°C/min, 500°C at TT1 and 600 °C in Sulphur at TT2 results in bandgap energy of 1.58 eV.

Nonetheless, there is much room for improvement. For example, the process can be optimized in terms of thickness. Besides that, a preliminary study is being carried out to understand the effect of grain growth on different substrates like silicon (Si), molybdenum (Mo) and fluorine doped tin oxide (FTO).

In the second section of the report we show that it is possible to produce kesterite ($\text{Cu}_2\text{ZnSnS}_4$) powders using an alternative process with a cost even lower than “hot-injection”: high-energy ball milling. Starting from a mixture of the elementary components of kesterite, Cu, Sn, Zn and S, in stoichiometric proportions it was possible to obtain a CZTS phase by reactive grinding in a high-energy planetary ball mill. The grinding bodies of brass (a Cu-Zn alloy) limit the contamination, which appears only for prolonged grinding times. The CZTS thus produced is characterized by finely dispersed crystalline domains, of the order of 1-2 nm, which take a cubic instead of the stable tetragonal form, probably because of the high disorder in cation positioning and low temperature process which inhibits diffusion.

As shown in Figure 29, it is possible to find a broad time range over which the amount of CZTS is close to 100%; longer times lead to contamination from the brass vials. However, this contamination can be reduced or eliminated altogether in the next future by: (i) optimization of the milling process, like amount of powder, size of the balls, milling time and jar rotation / disk revolution speeds; (ii) addition of suitable lubricants, also in view of a production of a solar ink, ready to be deposited on substrates for thin film production; (iii) use of balls and jars of different materials: so far we are considering the use of WC and zirconia. The work is in progress.

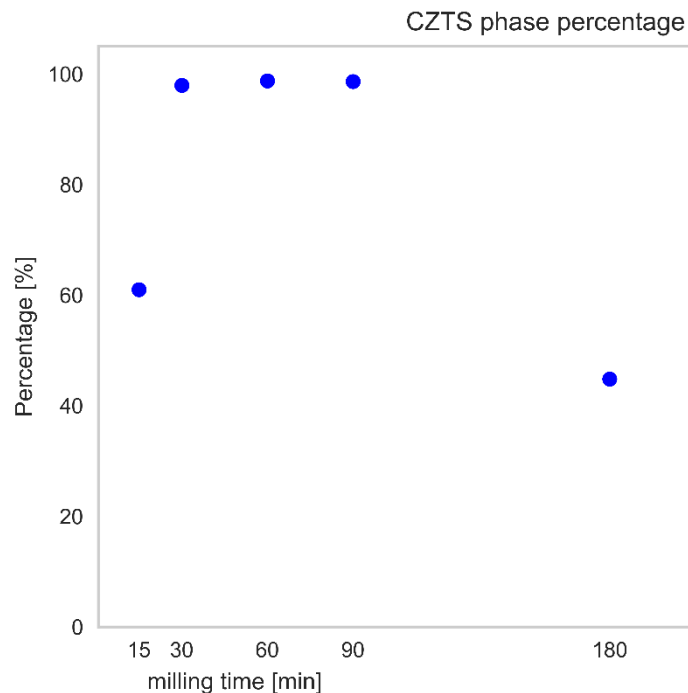


Figure 29 Percentage of CZTS phase formed by high-energy reactive grinding for increasing process time

References

- [1] A. Fairbrother, X. Fontané, V. Izquierdo-Roca, M. Espindola-Rodriguez, S. López-Marino, M. Placidi, J. López-García, A. Pérez-Rodríguez e E. Saucedo, «Single-Step Sulfo-Selenization Method to Synthesize $\text{Cu}_2\text{ZnSn}(\text{S}_y\text{Se}_{1-y})_4$ Absorbers from Metallic Stack Precursors,» *ChemPhysChem*, vol. 14, pp. 1836-1843, 2013.
- [2] A. Fairbrother, E. García-Hemme, V. Izquierdo-Roca, X. Fontané, F. A. Pulgarín-Agudelo, O. Vigil-Galán, A. Pérez-Rodríguez e E. Saucedo, «Development of a Selective Chemical Etch To Improve the Conversion Efficiency of Zn-Rich $\text{Cu}_2\text{ZnSnS}_4$ Solar Cells,» *Journal of the American Chemical Society*, vol. 134, pp. 8018-8021, 2012.
- [3] W. Wang, M. T. Winkler, O. Gunawan, T. Gokmen, T. K. Todorov, Y. Zhu e D. B. Mitzi, «Device Characteristics of CZTSSe Thin-Film Solar Cells with 12.6% Efficiency,» *Advanced Energy Materials*, vol. 4, p. 1301465, 2014.
- [4] G. Chen, C. Yuan, J. Liu, Y. Deng, G. Jiang, W. Liu e C. Zhu, «Low cost preparation of $\text{Cu}_2\text{ZnSnS}_4$ and

- Cu₂ZnSn(S_xSe_{1-x})₄ from binary sulfide nanoparticles for solar cell application,» *Journal of Power Sources*, vol. 262, pp. 201-206, 2014.
- [5] D. B. Mitzi, *Solution processing of inorganic materials*, Wiley, 2009.
- [6] H. Yang, L. A. Jauregui, G. Zhang, Y. P. Chen e Y. Wu, «Nontoxic and Abundant Copper Zinc Tin Sulfide Nanocrystals for Potential High-Temperature Thermoelectric Energy Harvesting,» *Nano Letters*, vol. 12, pp. 540-545, 2012.
- [7] S. E. Habas, H. A. S. Platt, M. F. A. M. Hest e D. S. Ginley, «Low-Cost Inorganic Solar Cells: From Ink To Printed Device,» *Chemical Reviews*, vol. 110, pp. 6571-6594, 2010.
- [8] S. Abermann, «Non-vacuum processed next generation thin film photovoltaics: Towards marketable efficiency and production of CZTS based solar cells,» *Solar Energy*, vol. 94, pp. 37-70, 8 2013.
- [9] M. Jiang e X. Yan, «Cu₂ZnSnS₄ Thin Film Solar Cells: Present Status and Future Prospects,» in *Solar Cells*, A. Morales-Acevedo, A cura di, Rijeka, IntechOpen, 2013.
- [10] D. Aldakov, A. Lefrançois e P. Reiss, «Ternary and quaternary metal chalcogenide nanocrystals: synthesis, properties and applications,» *Journal of Materials Chemistry C*, vol. 1, p. 3756, 2013.
- [11] N. Ataollahi, C. Malerba, E. Cappelletto, R. Ciancio, R. Edla, R. D. Maggio e P. Scardi., «Control of composition and grain growth in Cu₂ZnSnS₄ thin films from nanoparticle inks (submitted article),» *Thin Solid Films*, 2018.
- [12] D. Xia, P. Lei, Y. Zheng e B. Zhou, «Synthesis and characterization of Cu₂ZnSnS₄ nanocrystals by hot-injection method,» *Journal of Materials Science: Materials in Electronics*, vol. 26, pp. 5426-5432, 01 7 2015.
- [13] A. Singh, H. Geaney, F. Laffir e K. M. Ryan, «Colloidal Synthesis of Wurtzite Cu₂ZnSnS₄ Nanorods and Their Perpendicular Assembly,» *Journal of the American Chemical Society*, vol. 134, pp. 2910-2913, 2012.
- [14] A. Soosaimanickam, R. Jeyagopal, Y. Hayakawa e M. B. Sridharan, «Synthesis of oleylamine-capped Cu₂ZnSn(S,Se)₄ nanoparticles using 1-dodecanethiol as sulfur source,» *Japanese Journal of Applied Physics*, vol. 54, p. 08KA10, 2015.
- [15] N. Mirbagheri, S. Engberg, A. Crovetto, S. B. Simonsen, O. Hansen, Y. M. Lam e J. Schou, «Synthesis of ligand-free CZTS nanoparticles via a facile hot injection route,» *Nanotechnology*, vol. 27, p. 185603, 2016.
- [16] S. Schorr, A. Weber, V. Honkimäki e H.-W. Schock, «In-situ investigation of the kesterite formation from binary and ternary sulphides,» *Thin Solid Films*, vol. 517, pp. 2461-2464, 2009.
- [17] S. Chen, X. G. Gong, A. Walsh e S.-H. Wei, «Defect physics of the kesterite thin-film solar cell absorber Cu₂ZnSnS₄,» *Applied Physics Letters*, vol. 96, p. 021902, 2010.
- [18] C. Huang, Y. Chan, F. Liu, D. Tang, J. Yang, Y. Lai, J. Li e Y. Liu, «Synthesis and characterization of multicomponent Cu₂(Fe x Zn 1- x)SnS₄ nanocrystals with tunable band gap and structure,» *Journal of Materials Chemistry A*, vol. 1, pp. 5402-5407, 2013.
- [19] V. Kheraj, K. K. Patel, S. J. Patel e D. V. Shah, «Synthesis and characterisation of Copper Zinc Tin Sulphide (CZTS) compound for absorber material in solar-cells,» *Journal of Crystal Growth*, vol. 362, pp. 174-177, 2013.
- [20] A. G. Kannan, T. E. Manjulavalli e J. Chandrasekaran, «Influence of Solvent on the Properties of CZTS Nanoparticles,» *Procedia Engineering*, vol. 141, pp. 15-22, 2016.
- [21] K. Diwate, K. Mohite, M. Shinde, S. Rondiya, A. Pawbake, A. Date, H. Pathan e S. Jadkar, «Synthesis and Characterization of Chemical Spray Pyrolysed CZTS Thin Films for Solar Cell Applications,» *Energy Procedia*, vol. 110, pp. 180-187, 2017.
- [22] P. A. Fernandes, P. M. P. Salomé e A. F. Cunha, «Study of polycrystalline Cu₂ZnSnS₄ films by Raman scattering,» *Journal of Alloys and Compounds*, vol. 509, pp. 7600-7606, 2011.
- [23] W. C. Liu, B. L. Guo, X. S. Wu, F. M. Zhang, C. L. Mak e K. H. Wong, «Facile hydrothermal synthesis of

hydrotropic Cu₂ZnSnS₄ nanocrystal quantum dots: band-gap engineering and phonon confinement effect,» *J. Mater. Chem. A*, vol. 1, n. 9, pp. 3182-3186, 2013.

- [24] H. Suarez, J. M. Correa, S. D. Cruz, C. A. Otalora, M. Hurtado e G. Gordillo, «Synthesis and study of properties of CZTS thin films grown using a novel solution-based chemical route,» in *Photovoltaic Specialists Conference (PVSC), 2013 IEEE 39th*, 2013.
- [25] G. Gordillo, C. Calderón e P. Bartolo-Pérez, «XPS analysis and structural and morphological characterization of Cu₂ZnSnS₄ thin films grown by sequential evaporation,» *Applied Surface Science*, vol. 305, pp. 506-514, 2014.
- [26] O. Madelung, U. Rössler e M. Schulz, A cura di, *Tin sulfide (SnS) band structure, energy gaps: Datasheet from Landolt-Börnstein - Group III Condensed Matter Volume 41C: ``Non-Tetrahedrally Bonded Elements and Binary Compounds I'' in SpringerMaterials (<https://dx.doi.org/10.1007/10681727837>)*, Springer-Verlag Berlin Heidelberg.
- [27] P. Sharma, I. Sharma e S. C. Katyal, «Physical and optical properties of binary amorphous selenium-antimony thin films,» *Journal of Applied Physics*, vol. 105, p. 053509, 2009.
- [28] H. K. Teoman Özdal, «Determination of crystallization threshold temperature for sol-gel spin,» *Ceramics International*, vol. 44, p. 18928–18934, 2018.
- [29] Q. Xu, B. Huang, Y. Zhao, Y. Yan, R. Noufi e S.-H. Wei, «Crystal and electronic structures of Cu_xS solar cell absorbers,» *Applied Physics Letters*, vol. 100, p. 061906, 2012.
- [30] H. Yoo, J. Kim e L. Zhang, «Sulfurization temperature effects on the growth of Cu₂ZnSnS₄ thin film,» *Current Applied Physics*, vol. 12, pp. 1052-1057, 2012.
- [31] B. D. Chernomordik, A. E. Béland, D. D. Deng, L. F. Francis e E. S. Aydil, «Microstructure Evolution and Crystal Growth in Cu₂ZnSnS₄ Thin Films Formed By Annealing Colloidal Nanocrystal Coatings,» *Chemistry of Materials*, vol. 26, pp. 3191-3201, 2014.
- [32] M. Broseghini, L. Gelisio, M. D’Incau, C. L. A. Ricardo, N. M. Pugno e P. Scardi, «Modeling of the planetary ball-milling process: The case study of ceramic powders,» *Journal of the European Ceramic Society*, vol. 36, pp. 2205-2212, 2016.
- [33] P. Scardi, «Chapter 13 Microstructural Properties: Lattice Defects and Domain Size Effects,» in *Powder Diffraction: Theory and Practice*, The Royal Society of Chemistry, 2008, pp. 376-413.
- [34] P. Scardi, C. L. Azanza Ricardo, C. Perez-Demydenko e A. A. Coelho, «Whole powder pattern modelling macros for,» *Journal of Applied Crystallography*, vol. 51, 12 2018.
- [35] C. L. Azanza Ricardo, F. Girardi, E. Cappelletto, R. D’Angelo, R. Ciancio, E. Carlino, P. C. Ricci, C. Malerba, A. Mittiga, R. Di Maggio e P. Scardi, «Chloride-based route for monodisperse Cu₂ZnSnS₄ nanoparticles preparation,» *Journal of Renewable and Sustainable Energy*, vol. 7, p. 043150, 2015.
- [36] C. J. Bosson, M. T. Birch, D. P. Halliday, K. S. Knight, A. S. Gibbs e P. D. Hatton, «Cation disorder and phase transitions in the structurally complex solar cell material Cu₂ZnSnS₄,» *Journal of Materials Chemistry A*, vol. 5, pp. 16672-16680, 2017.
- [37] S. Schorr e G. Gonzalez-Aviles, «In-situ investigation of the structural phase transition in kesterite,» *physica status solidi (a)*, vol. 206, pp. 1054-1058, 2009.
- [38] S. Schorr, «The crystal structure of kesterite type compounds: A neutron and X-ray diffraction study,» *Solar Energy Materials and Solar Cells*, vol. 95, pp. 1482-1488, 2011.
- [39] M.-L. Liu, F.-Q. Huang, L.-D. Chen e I.-W. Chen, «A wide-band-gap p-type thermoelectric material based on quaternary chalcogenides of Cu₂ZnSnQ₄ (Q=S,Se),» *Applied Physics Letters*, vol. 94, p. 202103, 2009.
- [40] S. Kumar, M. Z. Ansari e N. Khare, «Enhanced thermoelectric power factor of Cu₂ZnSnS₄ in the presence of Cu₂-xS and SnS₂ secondary phase,» *AIP Conference Proceedings*, vol. 1832, p. 120033, 2017.
- [41] S. Kumar, M. Z. Ansari e N. Khare, «Influence of compactness and formation of metallic secondary

phase on the thermoelectric properties of Cu₂ZnSnS₄ thin films,» *Thin Solid Films*, vol. 645, pp. 300-304, 2018.

Abbreviazioni ed acronimi

CZTS Copper zinc tin sulfide

DICAM Dipartimento di Ingegneria Civile Ambientale e Meccanica

EDXS Energy dispersive X-ray spectroscopy

HAADF-STEM High angle annular dark field- scanning transmission electron microscopy

HRTEM High resolution transmission electron microscopy

SEM scanning electron microscopy

TT1 Primo trattamento termico

TT2 Secondo trattamento termico

XRF X-ray fluorescence spectroscopy

GDOES Glow Discharge Optical Emission Spectroscopy

Curriculum scientifico del gruppo dell'Università di Trento.

Il gruppo del Prof. Scardi lavora da anni sulle tecniche di diffrattometria per la caratterizzazione della microstruttura, della tessitura e degli stress residui in materiali sia metallici che ceramici, anche in forma di film sottili. Si è occupato sia dello sviluppo di software per la modellazione degli spettri che dell'uso di sorgenti non convenzionali (radiazione di sincrotrone, neutroni) collaborando alla progettazione e realizzazione della nuova beamline (MCX) per la diffrazione dei raggi X da film sottili, rivestimenti e materiali policristallini, presso il sincrotrone italiano (ELETTRA, Trieste). Recentemente il gruppo si è anche dedicato allo sviluppo di tecniche di deposizione dei film sottili sia con metodi fisici (PVD) che chimici (CBD, sol-gel, spin-coating).